Improved fully implicit discrete-velocity method for efficient simulation of flows in all flow regimes

L. M. Yang,[1] Z. Chen,[1] C. Shu,[1,*] W. M. Yang,[1] J. Wu,[2] and L. Q. Zhang[1]

[1]*Department of Mechanical Engineering, National University of Singapore, 10 Kent Ridge Crescent, Singapore 119260*

[2]*Department of Aerodynamics, College of Aerospace Engineering, Nanjing University of Aeronautics and Astronautics, Yudao Street, Nanjing 210016, Jiangsu, China*

(Received 5 October 2018; published 26 December 2018)

In this work, an improved fully implicit discrete-velocity method (DVM) is developed for flows over all Knudsen numbers. The improvements aim to overcome the drawbacks of the conventional semi-implicit DVM which performs with low accuracy and efficiency in the continuum flow regime. These defects originate from the explicit discretization of the equilibrium state in the collision term at the cell center and the ignorance of the particle collision effect in the calculation of numerical flux on the cell interface. To alleviate these drawbacks, the present method innovatively incorporates an implicit prediction step into the conventional model. In this step, the macroscopic governing equation is resolved to estimate the equilibrium state, and the local solution of the Boltzmann equation with the collision term is adopted to physically reconstruct the macroscopic numerical flux. Two major merits are brought by this strategy. On one hand, by using the predicted equilibrium state, the collision term in the discrete velocity Boltzmann equation can be discretized implicitly, which significantly improves the computational efficiency. On the other hand, the consideration of the collision effect in the physical reconstruction of the numerical flux on the cell interface benefits the solution accuracy, especially in the continuum flow regime. Meanwhile, the developed scheme well keeps the inherent simplicity of the conventional semi-implicit DVM by maintaining the basic resolving process of distribution functions. Numerical results show that in the rarefied flow regime, the improved scheme gives a similar solution as the conventional semi-implicit DVM with little extra computational efforts, while in the continuum flow regime, the present scheme shows higher efficiency and accuracy.

DOI: 10.1103/PhysRevE.98.063313

I. INTRODUCTION

The degree of gas rarefaction is usually characterized by the Knudsen (Kn) number, which is defined as the ratio of the mean free path to the characteristic length [1]. In practical engineering problems, the local Knudsen number may vary significantly over several orders of magnitude. As shown in the work of Jiang [2] and Xu and Liu [3], for hypersonic flow around a flying vehicle at Mach number $\mathrm{Ma} = 4$ and Reynolds number $\mathrm{Re} = 59\,373$, the minimum and maximum local Knudsen numbers are, respectively, 7.61×10^{-5} and 19.9. Such vast variation of Knudsen number means that various flow physics ranging from the free molecular flow regime ($\mathrm{Kn} \geqslant 10$) to the continuum flow regime ($\mathrm{Kn} < 10^{-2}$) simultaneously exist in different parts of the vehicle. Experimental investigation of such flow problems is very difficult and expensive in the current stage. Numerical simulation is thus a preferable solution. To do that, it is necessary to develop an accurate and efficient numerical method for all Knudsen number flows.

The Boltzmann equation describes the time evolution of the gas distribution function, which is completely free from the continuum assumption. Thus, it is theoretically possible to develop a numerical method for the solution of the Boltzmann equation that is valid over the full spectrum of flow regimes. Resolving the Boltzmann equation requires numerical integration over the particle velocity space. In practice, the infinite particle velocity space is usually truncated to a certain region and discretized by a set of discrete-velocity points [4–8]. The resulting governing equation is commonly known as the discrete-velocity Boltzmann equation (DVBE) and the numerical method for solving the DVBE is generally called the discrete-velocity method (DVM) or the discrete ordinate method (DOM) [9–13]. In DVM, the finite volume method (FVM) is frequently used to discretize the DVBE, while the numerical flux at the cell interface and the collision term of DVBE at the cell center are calculated by different ways.

In the conventional DVM, the numerical flux is usually computed by the upwind scheme in which only the particle transport process is considered [4,5,10,14–18]. This process is equivalent to reconstructing the numerical flux by solving the collisionless Boltzmann equation on the cell interface. The motivation for this strategy is to simplify the implementation. Such simplification can provide accurate and efficient prediction for high Knudsen number flows in which the particle free transport mechanism dominates the solutions, but will deteriorate the solution accuracy for the simulation of continuum flows. The reason for the deterioration is that the ignored particle collisions would intensively take place in this flow regime and have a significant effect on the solution. Too much numerical dissipation is thus introduced by the simplification, due to which very fine mesh size (of the order of the mean free path) is needed to ensure accuracy. For the

*Corresponding author: mpeshuc@nus.edu.sg

purpose of improving computational efficiency, explorations have been made to incorporate the implicit technique into the conventional DVM [10,19–22]. The essential issue in implicit manipulation is to approximate the equilibrium state at the new time level g^{n+1}, which is utilized in implicit discretization of the collision term. By simply approximating g^{n+1} with g^n, an implicit DVM was developed by Yang and Huang [10] and Aoki *et al.* [19]. A similar strategy was used by Titarev [20,21] to propose an implicit DVM for rarefied flows on unstructured meshes. In fact, these methods could be categorized into semi-implicit DVM since only the loss term $-f$ (because it gives negative distribution) is treated implicitly in the collision term and the equilibrium state g (the gain term) is still discretized explicitly. As commented by Mieussens [22], the decoupling of the gain and the loss terms may slow down the convergence rate considerably in the continuum flow regime. To overcome this drawback, Mieussens [22] approximated g^{n+1} by a mapping between the equilibrium state g^n and the gas distribution functions f^n and f^{n+1}, and then developed a linearized implicit DVM for the simulation of rarefied flows. In his method, the mapping corresponds to a Jacobian matrix in the scale of the number of discrete-velocity points, which significantly complicates the algorithm.

Apart from the exploration in the implicit time-marching scheme, special attention has been paid to improve the accuracy and efficiency of the conventional DVM in the continuum flow regime. Two representative outcomes are the unified gas kinetic scheme (UGKS) [3,6,23–26] and the discrete unified gas kinetic scheme (DUGKS) [27–30]. These two schemes are both developed within the framework of DVM, but utilize the local solution of Boltzmann equation with the collision term to reconstruct the numerical fluxes on the cell interface. The consideration of the collision effect endows these two schemes with higher robustness in physics. Correspondingly, they can give reasonable prediction of flow prosperities over all flow regimes. In addition, since the macroscopic and the microscopic governing equations are solved simultaneously at each time step in UGKS, g^{n+1} can be easily estimated from the solution of the macroscopic governing equation. Accordingly, the fully implicit discretization can be implemented straightforwardly when solving the DVBE. By introducing the classical lower-upper symmetric Gauss-Seidel (LU-SGS) method to solve both the macroscopic and the microscopic governing equations, a fully implicit UGKS was constructed by Zhu *et al.* [31] recently. In their method, the drawback of low convergence rate in the continuum flow regime of the conventional semi-implicit DVM is overcome effectively. However, this scheme needs to calculate the local integral solution of the Boltzmann equation on the cell interface when resolving the DVBE, which complicates the computation and sacrifices the efficiency of the conventional DVM [4,5,10,14–18] in the rarefied flow regime.

From the above discussions, we can see that the existing DVM or DVM-based algorithms (UGKS or DUGKS) cannot well balance the numerical accuracy and the efficiency in different flow regimes. The conventional DVM performs poorly in the continuum flow regime because it ignores the particle collision effect in reconstructing numerical fluxes. UGKS or DUGKS could fix this flaw and give accurate predictions in the continuum flow regime, but trade off the simplicity and computational efficiency in rarefied flow regime [32]. The motivation of the present work is to develop an improved implicit DVM which ensures the accuracy and efficiency over all flow regimes. To overcome the defect of low efficiency of the conventional semi-implicit DVM in the continuum flow regime, an implicit prediction step is introduced in the improved model to estimate the equilibrium state, which enables the implicit discretization of the collision term in DVBE. In the prediction step, the macroscopic governing equation recovered from the Boltzmann equation is solved by the classical LU-SGS method. Furthermore, to overcome the drawback of poor accuracy of the conventional semi-implicit DVM in the continuum flow regime, the macroscopic numerical fluxes on the cell interface are reconstructed from the physical solution with the collision effect. Meanwhile, since the collision effect has a negligible effect on the solution in the highly rarefied flow regime [33,34], the conventional approach of reconstructing microscopic numerical flux in the DVBE is adopted to keep the inherent simplicity of conventional DVM. In other words, the upwind scheme is still adopted to evaluate numerical fluxes in the evolution of distribution functions. Further analyses performed in this paper will show that the physically reconstructed numerical flux in the macroscopic equation is actually a self-adaptive combination of the microscopic reconstruction from the collisionless Boltzmann solver (conventional DVM) and the macroscopic reconstruction from the Navier-Stokes solver [35–38]. The derived adaptive parameter turns out to be a function of the physical time step Δt_p and the collision timescale τ, which mathematically interprets the relative importance of the collision effect in various flow regimes. In the rarefied flow regime, the macroscopic part has almost no effect on the reconstruction of numerical flux since $\Delta t_p \ll \tau$, while it plays an important role in the continuum flow regime. As a result, the developed scheme shows great flexibility: it converges toward the conventional DVM in the free molecular flow regime and approaches to the Navier-Stokes solver in the continuum flow regime. Such characteristic fulfills our initial expectation that the improved implicit DVM can give accurate and efficient solutions to various problems over the whole flow regimes. The performance of the developed scheme will be validated by its application to several flow problems from the free molecular flow regime to the continuum flow regime.

II. GOVERNING EQUATIONS

The present work starts from the Boltzmann equation with the Bhatnagar-Gross-Krook-Shakhov (BGK-Shakhov) model [39], which reads

$$\frac{\partial f}{\partial t} + \boldsymbol{\xi} \cdot \nabla f = \frac{f^{\mathrm{eq}} - f}{\tau}, \tag{1}$$

where $f(\mathbf{x}, \boldsymbol{\xi}, \boldsymbol{\eta}, \boldsymbol{\zeta}, t)$ is the gas distribution function that depends on the physical space $\mathbf{x} = (x_1, \ldots, x_D)$, particle velocity space $(\boldsymbol{\xi}, \boldsymbol{\eta}, \boldsymbol{\zeta})$, and time t. Here, $\boldsymbol{\xi} = (\xi_1, \ldots, \xi_D)$ is the particle velocity in D-dimensional space; $\boldsymbol{\eta} = (\xi_{D+1}, \ldots, \xi_3)$ is a vector of dimension $(3 - D)$ consisting of the rest components of the particle velocity (ξ_1, ξ_2, ξ_3) in three-dimensional space; and $\boldsymbol{\zeta} = (\zeta_1, \ldots, \zeta_N)$ is a vector of dimension N representing the internal degree of freedom of molecules. The heat

specific ratio γ is determined by $\gamma = (N+5)/(N+3)$. $f^{\rm eq}$ is the equilibrium state approached by f through particle collisions within a collision timescale τ. For the BGK-Shakhov model, the equilibrium state $f^{\rm eq}$ can be written as

$$f^{\rm eq} = f_M^{\rm eq}\left[1 + (1-{\rm Pr})\frac{\mathbf{c}\cdot\mathbf{q}}{5pRT}\left(\frac{c^2+\eta^2}{RT} - 5\right)\right]. \quad (2)$$

Here, $f_M^{\rm eq}$ is the Maxwellian distribution function given by

$$f_M^{\rm eq} = \frac{\rho}{(2\pi RT)^{(3+N)/2}}\exp\left[-\frac{c^2+\eta^2+\zeta^2}{2RT}\right], \quad (3)$$

and Pr is the Prandtl number. $\mathbf{c} = \boldsymbol{\xi} - \mathbf{u}$ is the peculiar velocity of the particle, $\mathbf{u}$ is the velocity of the mean flow, $\mathbf{q}$ is the heat flux, R is the gas constant, ρ is the density, p is the pressure, and T is the temperature. Note that in this work, the vector is expressed by the bold style and its magnitude is represented by the italic style (such as $c = |\mathbf{c}|$). It can be seen from Eq. (2) that the equilibrium state $f^{\rm eq}$ is fully determined by the macroscopic flow variables.

The relations between the conservative variables $\mathbf{W}$, heat flux $\mathbf{q}$, stress tensor $\boldsymbol{\tau}$, and the distribution function f are as follows:

$$\mathbf{W} = (\rho, \rho\mathbf{u}, \rho E)^T = \int \boldsymbol{\psi} f d{\rm E}, \quad (4)$$

$$\mathbf{q} = \frac{1}{2}\int \mathbf{c}(c^2+\eta^2+\zeta^2) f d{\rm E}, \quad (5)$$

$$\boldsymbol{\tau} = \int \mathbf{cc} f d{\rm E} - p\mathbf{I}, \quad (6)$$

where $\boldsymbol{\psi} = [1, \boldsymbol{\xi}, (\xi^2+\eta^2+\zeta^2)/2]^T$ is the moment, $d{\rm E} = d\boldsymbol{\xi}d\boldsymbol{\eta}d\boldsymbol{\zeta}$ is the volume element in the particle velocity space, and $\mathbf{I}$ is the unit tensor. In order to solve Eq. (1) numerically, the particle velocity space should be discretized into a set of discrete velocities $\boldsymbol{\xi}_\alpha$, $(\alpha = 1, \ldots, N_V)$. The resultant equation is the DVBE given by

$$\frac{\partial f_\alpha}{\partial t} + \boldsymbol{\xi}_\alpha \cdot \nabla f_\alpha = \frac{f_\alpha^{\rm eq} - f_\alpha}{\tau}, \quad (7)$$

where f_α and $f_\alpha^{\rm eq}$ are the discrete distribution function and its equilibrium state along the direction of discrete particle velocity $\boldsymbol{\xi}_\alpha$. In the practical calculation, two reduced distribution functions are often introduced to replace the distribution function f_α in order to save the virtual memory and computational effort since the evolution of f_α depends only on the D-dimensional particle velocity $\boldsymbol{\xi}$ and is irrelevant to $\boldsymbol{\eta}$ and $\boldsymbol{\zeta}$. The details can be found in Refs. [9,13,28].

III. CONVENTIONAL SEMI-IMPLICIT DVM FOR SOLVING DVBE

Before introducing the improved implicit DVM, the conventional semi-implicit DVM is briefly reviewed. The term "semi-implicit" comes from the fact that only the loss term is discretized implicitly and the equilibrium state is still calculated explicitly in the conventional model [10,19–21]. In general, the semi-implicit discretization form of Eq. (7) can be written as

$$\frac{f_\alpha^{n+1} - f_\alpha^n}{\Delta t} + \boldsymbol{\xi}_\alpha \cdot \nabla f_\alpha^{n+1} = \frac{f_\alpha^{{\rm eq},n} - f_\alpha^{n+1}}{\tau^n}, \quad (8)$$

where the superscript n represents the current iteration step. Δt is the time step for implicit discretization determined by

$$\Delta t = \sigma\frac{\Delta x}{\xi_{\max} + c_s}. \quad (9)$$

Here, σ is the associated Courant-Friedrichs-Lewy (CFL) number, which can be set larger than one to achieve higher efficiency. $\xi_{\max}$ is the maximum discrete particle velocity, Δx is the grid spacing, and c_s is the sound speed. To solve Eq. (8), the following delta form of the distribution function is commonly adopted:

$$\Delta f_\alpha^{n+1} = f_\alpha^{n+1} - f_\alpha^n. \quad (10)$$

By substituting Eq. (10) into Eq. (8), we have

$$\frac{\Delta f_\alpha^{n+1}}{\Delta t} + \frac{\Delta f_\alpha^{n+1}}{\tau^n} + \boldsymbol{\xi}_\alpha \cdot \nabla\left(\Delta f_\alpha^{n+1}\right) = \frac{f_\alpha^{{\rm eq},n} - f_\alpha^n}{\tau^n} - \boldsymbol{\xi}_\alpha \cdot \nabla f_\alpha^n. \quad (11)$$

Integrating Eq. (11) over a control volume V yields

$$\left(\frac{1}{\Delta t} + \frac{1}{\tau^n}\right)\int_V \Delta f_\alpha^{n+1} dV + \int_{\partial V} \mathbf{n}\cdot\boldsymbol{\xi}_\alpha \Delta f_{\partial V,\alpha}^{n+1} dS = {\rm Res}_\alpha^n, \quad (12)$$

where ${\rm Res}_\alpha^n$ is the microscopic residual given by

$${\rm Res}_\alpha^n = \frac{1}{\tau^n}\int_V \left(f_\alpha^{{\rm eq},n} - f_\alpha^n\right) dV - \int_{\partial V} \mathbf{n}\cdot\boldsymbol{\xi}_\alpha f_{\partial V,\alpha}^n dS. \quad (13)$$

Here, $\mathbf{n}$ denotes the outward normal vector on the surface of the control volume, and ∂V represents the surface of the control volume.

Since Δf_α^{n+1} eventually reduces to zero for steady flow problems, $\Delta f_{\partial V,\alpha}^{n+1}$ on the left-hand side of Eq. (12) can be simply approximated by the first-order upwind scheme to obtain a simpler iteration scheme. As a result, the discretized form of Eq. (12) in grid cell i can be written as

$$\left(\frac{V_i}{\Delta t_i} + \frac{V_i}{\tau_i^n} + \frac{1}{2}\sum_{j\in N(i)} |\mathbf{n}_{ij}\cdot\boldsymbol{\xi}_\alpha| S_{ij}\right)\Delta f_{i,a}^{n+1} + \frac{1}{2}\sum_{j\in N(i)} (\mathbf{n}_{ij}\cdot\boldsymbol{\xi}_\alpha - |\mathbf{n}_{ij}\cdot\boldsymbol{\xi}_\alpha|) S_{ij}\Delta f_{j,a}^{n+1} = {\rm Res}_{i,\alpha}^n \quad (14)$$

and

$${\rm Res}_{i,\alpha}^n = \frac{V_i}{\tau_i^n}\left(f_{i,\alpha}^{{\rm eq},n} - f_{i,\alpha}^n\right) - \sum_{j\in N(i)} \mathbf{n}_{ij}\cdot\boldsymbol{\xi}_\alpha S_{ij} f_{ij,a}^n. \quad (15)$$

Equation (14) can be simply written as

$$\mathbf{A}_{ij}\Delta f_{j,a}^{n+1} = {\rm Res}_{i,\alpha}^n, \quad (16)$$

where $N(i)$ denotes the set of neighboring cells of cell i, S_{ij} is the area of the interface shared by cell i and cell j, $\mathbf{n}_{ij}$ is the normal vector of the cell interface directing from cell i to cell j, and $\mathbf{A}_{ij}$ is the coefficient matrix derived

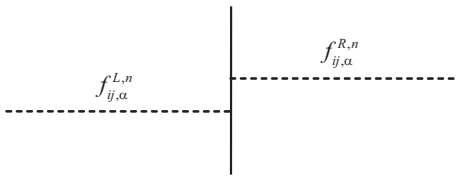

FIG. 1. Distribution function at the cell interface determined by the local solution of the collisionless Boltzmann equation with a piecewise constant distribution.

from Eq. (14). Equation (16) can be solved easily by using the classical lower-upper symmetric Gauss-Seidel (LU-SGS) method [40,41].

The second term on the right-hand side of Eq. (15) is the numerical flux of the distribution function at the cell interface. To calculate the numerical flux, the distribution function at the cell interface $f_{ij,a}^n$ should be determined in advance. In the conventional semi-implicit DVM, $f_{ij,a}^n$ is actually reconstructed from the local solution of following the collisionless Boltzmann equation with a piecewise constant distribution for the distribution function at the cell interface (see Fig. 1),

$$\frac{\partial f_\alpha}{\partial t} + \boldsymbol{\xi}_\alpha \cdot \nabla f_\alpha = 0, \tag{17a}$$

$$f(\mathbf{x}, \boldsymbol{\xi}_\alpha, 0) = \begin{cases} f_{ij,\alpha}^{L,n}, & \mathbf{n}_{ij} \cdot (\mathbf{x}_{ij} - \mathbf{x}) \geqslant 0 \\ f_{ij,\alpha}^{R,n}, & \mathbf{n}_{ij} \cdot (\mathbf{x}_{ij} - \mathbf{x}) < 0, \end{cases} \tag{17b}$$

where $\mathbf{x}_{ij} \in \partial V$ is the location of the midpoint on the cell interface shared by cell i and cell j. $f_{ij,\alpha}^{L,n}$ and $f_{ij,\alpha}^{R,n}$ are the piecewise constant distributions at the left and the right sides of the cell interface, which are calculated by the second-order scheme with slope limiter function in this work,

$$\begin{aligned} f_{ij,\alpha}^{L,n} &= f_{i,\alpha}^n + (\mathbf{x}_{ij} - \mathbf{x}_i) \cdot \boldsymbol{\sigma}_{i,\alpha}^n, \\ f_{ij,\alpha}^{R,n} &= f_{j,\alpha}^n + (\mathbf{x}_{ij} - \mathbf{x}_j) \cdot \boldsymbol{\sigma}_{j,\alpha}^n. \end{aligned} \tag{18}$$

Here, $\mathbf{x}_i$ and $\mathbf{x}_j$ are the coordinates of the cell centers of cell i and cell j, respectively. $\boldsymbol{\sigma}_{i,\alpha}^n$ and $\boldsymbol{\sigma}_{j,\alpha}^n$ are the slopes with the slope limiter of $f_{i,\alpha}^n$ and $f_{j,\alpha}^n$. In this study, the van Leer slope limiter [42] is adopted.

The solution of Eq. (17a) gives

$$f_{ij,a}^n = f(\mathbf{x}_{ij}, \boldsymbol{\xi}_\alpha, \Delta t_p) = f(\mathbf{x}_{ij} - \boldsymbol{\xi}_\alpha \Delta t_p, \boldsymbol{\xi}_\alpha, 0), \tag{19}$$

where Δt_p is the physical time step for calculation of the numerical flux, which is restrained by the following CFL condition:

$$\Delta t_p = \sigma_p \frac{\Delta x}{\xi_{\max} + c_s}. \tag{20}$$

Here, σ_p is the associated CFL number, which is less than one. Note that Δt_p is different from the time step for implicit iteration Δt in Eq. (9). In order to differ the distribution function computed by the local solution of the Boltzmann equation with the collision term, we denote the distribution function reconstructed from the collisionless Boltzmann equation by the subscript DVM hereinafter. By substituting Eq. (17b) into Eq. (19), we have

$$\begin{aligned} f_{ij,a}^n &= f_{\mathrm{DVM}}(\mathbf{x}_{ij}, \boldsymbol{\xi}_\alpha, \Delta t_p) \\ &= H(\mathbf{n}_{ij} \cdot \boldsymbol{\xi}_\alpha) f_{ij,\alpha}^{L,n} + [1 - H(\mathbf{n}_{ij} \cdot \boldsymbol{\xi}_\alpha)] f_{ij,\alpha}^{R,n}, \end{aligned} \tag{21}$$

where $H(\mathbf{n}_{ij} \cdot \boldsymbol{\xi}_\alpha)$ is the Heaviside function, $H(\mathbf{n}_{ij} \cdot \boldsymbol{\xi}_\alpha) = 1$ for $\mathbf{n}_{ij} \cdot \boldsymbol{\xi}_\alpha \geqslant 0$ and $H(\mathbf{n}_{ij} \cdot \boldsymbol{\xi}_\alpha) = 0$ for $\mathbf{n}_{ij} \cdot \boldsymbol{\xi}_\alpha < 0$. Once $f_{ij,\alpha}^n$ is obtained, the microscopic residual $\mathrm{Res}_{i,\alpha}^n$ can be calculated straightforwardly by Eq. (15) and the delta form of the distribution function is then determined by solving Eq. (16). Finally, the distribution functions at the cell centers are marched to a new time level $n+1$ via Eq. (10), and the macroscopic flow variables can be updated by Eqs. (4)–(6).

IV. IMPROVED FULLY IMPLICIT DVM FOR ALL KNUDSEN NUMBER FLOWS

A. Solution of microscopic and macroscopic governing equations

Two major defects have been recognized in the conventional semi-implicit DVM [10,19]. One defect is that the explicit discretization of the equilibrium state in the collision term may considerably slow down the convergence rate in the continuum flow regime [22]. The other defect is that the effect of particle collisions is ignored in the calculation of numerical flux on the cell interface. As commented by Xu [43], this treatment yields a direct single scale DVM, which requires a small cell size in comparison with the mean free path to get reasonable solutions. For the simulation of continuum flows at high Reynolds number, it is numerically challenging to satisfy such constraint since the mean free path is very small. Consequently, the conventional semi-implicit DVM gives less accurate results than the Navier-Stokes solver in the continuum flow regime.

In order to improve the computational efficiency and solution accuracy of the conventional semi-implicit DVM in the continuum flow regime, a fully implicit DVM is developed in this work. Different from the conventional semi-implicit DVM, both the gain and the loss terms are discretized implicitly in this method. As a result, Eq. (7) can be discretized as

$$\frac{f_\alpha^{n+1} - f_\alpha^n}{\Delta t} + \boldsymbol{\xi}_\alpha \cdot \nabla f_\alpha^{n+1} = \frac{\overline{f}_\alpha^{\mathrm{eq},n+1} - f_\alpha^{n+1}}{\tau^{n+1}}. \tag{22}$$

Similar to the solution process of Eq. (8), after introducing the delta form of the distribution function and integrating Eq. (22) over a control volume V, we have

$$\left(\frac{V_i}{\Delta t_i} + \frac{V_i}{\tau_i^{n+1}} + \frac{1}{2} \sum_{j \in N(i)} |\mathbf{n}_{ij} \cdot \boldsymbol{\xi}_\alpha| S_{ij} \right) \Delta f_{i,a}^{n+1} + \frac{1}{2} \sum_{j \in N(i)} (\mathbf{n}_{ij} \cdot \boldsymbol{\xi}_\alpha - |\mathbf{n}_{ij} \cdot \boldsymbol{\xi}_\alpha|) S_{ij} \Delta f_{j,a}^{n+1} = \overline{\mathrm{Res}}_{i,\alpha}^n, \tag{23}$$

with the microscopic residual of

$$\overline{\mathrm{Res}}_{i,\alpha}^n = \frac{V_i}{\tau_i^{n+1}} \left(\overline{f}_{i,\alpha}^{\mathrm{eq},n+1} - f_{i,\alpha}^n \right) - \sum_{j \in N(i)} \mathbf{n}_{ij} \cdot \boldsymbol{\xi}_\alpha S_{ij} f_{\mathrm{DVM}}(\mathbf{x}_{ij}, \boldsymbol{\xi}, \Delta t_p). \tag{24}$$

Equation (23) can also be solved by using the classical LU-SGS method [40,41]. As shown in Eq. (24), in the fully implicit DVM, the key is to calculate the predicted equilibrium state $\overline{f}_\alpha^{\mathrm{eq},n+1}$, which is equivalent to estimate conservative variables at the cell center at the new time level $\overline{\mathbf{W}}^{n+1}$.

To determine $\overline{\mathbf{W}}^{n+1}$, an implicit prediction step is introduced to solve the macroscopic governing equation. Taking conservative moments of Eq. (22), we have

$$\frac{\overline{\mathbf{W}}^{n+1}-\mathbf{W}^{n}}{\Delta t}+\nabla\cdot\mathbf{F}^{w,n+1}=0, \tag{25}$$

where $\mathbf{F}^{w,n+1}$ is the numerical flux of the macroscopic governing equation at time level $n+1$. When the LU-SGS method is utilized to solve Eq. (25), $\mathbf{F}^{w,n+1}$ can be linearized by the macroscopic numerical flux at time level n, which is given by

$$\mathbf{F}^{w,n}=\mathbf{F}^{w}(\mathbf{x},\Delta t_p)=\langle\boldsymbol{\xi}\boldsymbol{\psi}f^{n}\rangle_\alpha. \tag{26}$$

The symbol $\langle f\rangle_\alpha$ denotes the quadrature of f in the discrete velocity space, i.e., the summation, $\langle f\rangle_\alpha=\sum_{\alpha=1}^{N_V}w_\alpha f_\alpha$, where w_α is the associated quadrature weight at the discrete-velocity point $\boldsymbol{\xi}_\alpha$. When adopting the finite volume strategy to solve Eq. (25), it is essential to evaluate the flux $\mathbf{F}^{w,n}$ (or the distribution function f_α^n) on the cell interface. In UGKS [3,6,23–26], the particle transport process and its collision effect are considered simultaneously by reconstructing f_α^n from the local integral solution of DVBE. Since the flow variables and their derivatives at two sides of the cell interface are treated as discontinuous, a large number of coefficients related to the physical space and particle velocity space are necessary when performing numerical quadrature, which complicates the computation of UGKS as compared with the conventional DVM [10,19].

To preserve the simplicity of the conventional DVM, we propose an alternative strategy which only introduces the collision effect in the calculation of numerical flux of the macroscopic governing equation. The numerical fluxes of the macroscopic equation are physically reconstructed by the local solution of the Boltzmann equation with the collision term; and the solution of DVBE follows in the similar manner as the conventional DVM when reconstructing numerical fluxes. By integrating along the characteristic of Eq. (1), a local analytical solution on the cell interface can be derived [3,6,23–26]:

$$\begin{aligned}&f(\mathbf{x}_{ij},\boldsymbol{\xi}_\alpha,\Delta t_p)\\&=\frac{1}{\tau}\int_0^{\Delta t_p}f^{\mathrm{eq}}(\mathbf{x}_{ij}-\boldsymbol{\xi}_\alpha(\Delta t_p-t'),\boldsymbol{\xi}_\alpha,t')e^{-(\Delta t_p-t')/\tau}dt'\\&\quad+e^{-\Delta t_p/\tau}f(\mathbf{x}_{ij}-\boldsymbol{\xi}_\alpha\Delta t_p,\boldsymbol{\xi}_\alpha,0).\end{aligned} \tag{27}$$

The initial distribution function $f(\mathbf{x}_{ij}-\boldsymbol{\xi}_\alpha\Delta t_p,\boldsymbol{\xi}_\alpha,0)$ consists of the equilibrium and the nonequilibrium parts, i.e.,

$$\begin{aligned}f(\mathbf{x}_{ij}-\boldsymbol{\xi}_\alpha\Delta t_p,\boldsymbol{\xi}_\alpha,0)&=f^{\mathrm{eq}}(\mathbf{x}_{ij}-\boldsymbol{\xi}_\alpha\Delta t_p,\boldsymbol{\xi}_\alpha,0)\\&\quad+f_{\mathrm{DVM}}^{\mathrm{neq}}(\mathbf{x}_{ij}-\boldsymbol{\xi}_\alpha\Delta t_p,\boldsymbol{\xi}_\alpha,0),\end{aligned} \tag{28}$$

where $f_{\mathrm{DVM}}^{\mathrm{neq}}(\mathbf{x}_{ij}-\boldsymbol{\xi}_\alpha\Delta t_p,\boldsymbol{\xi}_\alpha,0)$ is the nonequilibrium distribution function in DVM. By substituting Eq. (28) into Eq. (27), we have

$$f(\mathbf{x}_{ij},\boldsymbol{\xi}_\alpha,\Delta t_p)=a+e^{-\Delta t_p/\tau}f_{\mathrm{DVM}}^{\mathrm{neq}}(\mathbf{x}_{ij}-\boldsymbol{\xi}_\alpha\Delta t_p,\boldsymbol{\xi}_\alpha,0), \tag{29}$$

with

$$\begin{aligned}a=&\frac{1}{\tau}\int_0^{\Delta t_p}f^{\mathrm{eq}}[\mathbf{x}_{ij}-\boldsymbol{\xi}_\alpha(\Delta t_p-t'),\boldsymbol{\xi}_\alpha,t']e^{-(\Delta t_p-t')/\tau}dt'\\&+e^{-\Delta t_p/\tau}f^{\mathrm{eq}}(\mathbf{x}_{ij}-\boldsymbol{\xi}_\alpha\Delta t_p,\boldsymbol{\xi}_\alpha,0).\end{aligned}$$

Similarly, if the continuum flow is considered, the distribution function on the cell interface can be expressed as

$$f_{\mathrm{NS}}(\mathbf{x}_{ij},\boldsymbol{\xi}_\alpha,\Delta t_p)=a+e^{-\Delta t_p/\tau}f_{\mathrm{NS}}^{\mathrm{neq}}(\mathbf{x}_{ij}-\boldsymbol{\xi}_\alpha\Delta t_p,\boldsymbol{\xi}_\alpha,0). \tag{30}$$

Here, $f_{\mathrm{NS}}(\mathbf{x}_{ij},\boldsymbol{\xi}_\alpha,\Delta t_p)$ and $f_{\mathrm{NS}}^{\mathrm{neq}}(\mathbf{x}_{ij}-\boldsymbol{\xi}_\alpha\Delta t_p,\boldsymbol{\xi}_\alpha,0)$ are the distribution function and its nonequilibrium part in the continuum limit, respectively.

Furthermore, according to Eq. (1), the nonequilibrium term $f_{\mathrm{DVM}}^{\mathrm{neq}}(\mathbf{x}_{ij}-\boldsymbol{\xi}_\alpha\Delta t_p,\boldsymbol{\xi}_\alpha,0)$ can be expressed as

$$f_{\mathrm{DVM}}^{\mathrm{neq}}(\mathbf{x}_{ij}-\boldsymbol{\xi}_\alpha\Delta t_p,\boldsymbol{\xi}_\alpha,0)=-\tau Df(\mathbf{x}_{ij}-\boldsymbol{\xi}_\alpha\Delta t_p,\boldsymbol{\xi}_\alpha,0), \tag{31}$$

where the operator D is $D=\partial_t+\boldsymbol{\xi}_\alpha\cdot\nabla$. By using the difference method, $f_{\mathrm{DVM}}^{\mathrm{neq}}(\mathbf{x}_{ij}-\boldsymbol{\xi}_\alpha\Delta t_p,\boldsymbol{\xi}_\alpha,0)$ can be approximated by

$$\begin{aligned}&f_{\mathrm{DVM}}^{\mathrm{neq}}(\mathbf{x}_{ij}-\boldsymbol{\xi}_\alpha\Delta t_p,\boldsymbol{\xi}_\alpha,0)\\&\quad=-\tau Df(\mathbf{x}_{ij},\boldsymbol{\xi}_\alpha,\Delta t_p)+O\big(\tau\Delta t_p,\xi_\alpha^2\tau\Delta t_p\big)\\&\quad=f_{\mathrm{DVM}}^{\mathrm{neq}}(\mathbf{x}_{ij},\boldsymbol{\xi}_\alpha,\Delta t_p)+O\big(\tau\Delta t_p,\xi_\alpha^2\tau\Delta t_p\big).\end{aligned} \tag{32}$$

Similarly, $f_{\mathrm{NS}}^{\mathrm{neq}}(\mathbf{x}_{ij}-\boldsymbol{\xi}_\alpha\Delta t_p,\boldsymbol{\xi}_\alpha,0)$ can be approximated by

$$\begin{aligned}&f_{\mathrm{NS}}^{\mathrm{neq}}(\mathbf{x}_{ij}-\boldsymbol{\xi}_\alpha\Delta t_p,\boldsymbol{\xi}_\alpha,0)\\&\quad=f_{\mathrm{NS}}^{\mathrm{neq}}(\mathbf{x}_{ij},\boldsymbol{\xi}_\alpha,\Delta t_p)+O\big(\tau\Delta t_p,\xi_\alpha^2\tau\Delta t_p\big).\end{aligned} \tag{33}$$

By applying Eqs. (32) and (33), the difference between Eq. (29) and Eq. (30) yields

$$\begin{aligned}&f(\mathbf{x}_{ij},\boldsymbol{\xi}_\alpha,\Delta t_p)\\&\quad=e^{-\Delta t_p/\tau}\big[f_{\mathrm{DVM}}^{\mathrm{neq}}(\mathbf{x}_{ij},\boldsymbol{\xi}_\alpha,\Delta t_p)-f_{\mathrm{NS}}^{\mathrm{neq}}(\mathbf{x}_{ij},\boldsymbol{\xi}_\alpha,\Delta t_p)\big]\\&\qquad+f_{\mathrm{NS}}(\mathbf{x}_{ij},\boldsymbol{\xi}_\alpha,\Delta t_p)+O\big(\tau\Delta t_p,\xi_\alpha^2\tau\Delta t_p\big).\end{aligned} \tag{34}$$

Besides that, the distribution function in Eq. (21) also consists of the equilibrium and the nonequilibrium parts:

$$\begin{aligned}&f_{\mathrm{DVM}}(\mathbf{x}_{ij},\boldsymbol{\xi}_\alpha,\Delta t_p)\\&\quad=f^{\mathrm{eq}}(\mathbf{x}_{ij},\boldsymbol{\xi}_\alpha,\Delta t_p)+f_{\mathrm{DVM}}^{\mathrm{neq}}(\mathbf{x}_{ij},\boldsymbol{\xi}_\alpha,\Delta t_p).\end{aligned} \tag{35}$$

By substituting Eq. (35) into Eq. (34) and noting that $f_{\mathrm{NS}}=f^{\mathrm{eq}}+f_{\mathrm{NS}}^{\mathrm{neq}}$, we have

$$\begin{aligned}f(\mathbf{x}_{ij},\boldsymbol{\xi}_\alpha,\Delta t_p)=&\,e^{-\Delta t_p/\tau}f_{\mathrm{DVM}}(\mathbf{x}_{ij},\boldsymbol{\xi}_\alpha,\Delta t_p)\\&+(1-e^{-\Delta t_p/\tau})f_{\mathrm{NS}}(\mathbf{x}_{ij},\boldsymbol{\xi}_\alpha,\Delta t_p)\\&+O\big(\tau\Delta t_p,\xi_\alpha^2\tau\Delta t_p\big).\end{aligned} \tag{36}$$

It can be seen from Eq. (36) that the accurate solution of the distribution function on the cell interface can be approximated by the weighted combination of the distribution function computed by the collisionless Boltzmann equation [Eq. (21)] and the solution from the Boltzmann equation which recovers the Navier-Stokes equation in the continuum regime with the truncation error of $O(\tau\Delta t_p, \xi_\alpha^2\tau\Delta t_p)$.

Accordingly, by substituting Eq. (36) into Eq. (26), we have

$$\begin{aligned}\mathbf{F}_{ij}^{w,n} &= \beta\langle\boldsymbol{\xi}\boldsymbol{\psi} f_{\mathrm{DVM}}(\mathbf{x}_{ij}, \boldsymbol{\xi}, \Delta t_p)\rangle_\alpha \\ &\quad + (1-\beta)\langle\boldsymbol{\xi}\boldsymbol{\psi} f_{\mathrm{NS}}(\mathbf{x}_{ij}, \boldsymbol{\xi}, \Delta t_p)\rangle_\alpha \\ &= \beta\mathbf{F}_{ij,DVM}^{w,n} + (1-\beta)\mathbf{F}_{ij,NS}^{w,n}, \end{aligned} \tag{37}$$

with an adaptive parameter of

$$\beta = e^{-\Delta t_p/\tau}, \tag{38}$$

where $\mathbf{F}_{ij}^{w,n} = \mathbf{F}^w(\mathbf{x}_{ij}, \Delta t_p)$. With Eq. (37), the numerical flux is divided into two components. The first part is evaluated by the collisionless solution which can be obtained by the previous strategy adopted in the conventional DVM; the other part is essentially the macroscopic flux $\mathbf{F}_{ij,NS}^{w,n}$, which is exactly the numerical flux in Navier-Stokes equations. Specifically, in this work, the inviscid part of $\mathbf{F}_{ij,NS}^{w,n}$ is evaluated by the commonly used Roe scheme, while its viscous part is calculated by the central difference scheme. The details can be found in Refs. [35,41].

Some important notions can be collected from Eqs. (37) and (38). In highly rarefied flows, τ is much larger than Δt_p, which yields that $\mathbf{F}_{ij,NS}^{w,n}$ has very little effect on the constructed numerical flux. Thus, this scheme is consistent with the conventional DVM in such regime. When simulating continuum flows, τ is far less than Δt_p, due to which $\mathbf{F}_{ij,NS}^{w,n}$ dominates the solutions. As a result, the developed scheme approaches to the Navier-Stokes solver in the continuum flow regime.

Once the numerical flux at the cell interface is obtained, implicit time-marching schemes (e.g., LU-SGS in the present work) can be adopted in Eq. (25) to achieve higher efficiency. For grid cell i, the implicit discretization form of Eq. (25) can be written as [33]

$$\left[\frac{V_i}{\Delta t_i}\mathbf{I} + \left(\frac{\partial\mathbf{R}}{\partial\mathbf{W}}\right)_i\right]\Delta\mathbf{W}_i^{n+1} = \mathbf{A}_w\Delta\mathbf{W}_i^{n+1} = -\mathbf{R}_i^n, \tag{39}$$

where $\Delta\mathbf{W}_i^{n+1} = \overline{\mathbf{W}}_i^{n+1} - \mathbf{W}_i^n$ is the solution correction and $\mathbf{A}_w$ denotes the system matrix. $\mathbf{R}_i^n$ is the macroscopic residual in cell i at time level of n, which is given by

$$\mathbf{R}_i^n = \sum_{j\in N(i)} \mathbf{n}_{ij}\cdot\mathbf{F}_{ij}^{w,n}S_{ij}. \tag{40}$$

$\mathbf{F}_{ij}^{w,n}$ is the numerical flux at the cell interface calculated by Eq. (37). $\partial\mathbf{R}/\partial\mathbf{W}$ is the flux Jacobian. In LU-SGS method, the flux Jacobian is usually approximated by the Euler equation-based flux splitting method to develop a matrix-free algorithm. As a result, Eq. (39) can be rewritten as

$$\begin{aligned}&\left(\frac{V_i}{\Delta t_i} + \frac{1}{2}\sum_{j\in N(i)} r_{ij}S_{ij}\right)\Delta\mathbf{W}_i^{n+1} \\ &\quad + \frac{1}{2}\sum_{j\in N(i)}\left[\mathbf{n}_{ij}\cdot\Delta\mathbf{F}_{c,j}^{n+1} - r_{ij}\Delta\mathbf{W}_j^{n+1}\right]S_{ij} = -\mathbf{R}_i^n, \end{aligned} \tag{41}$$

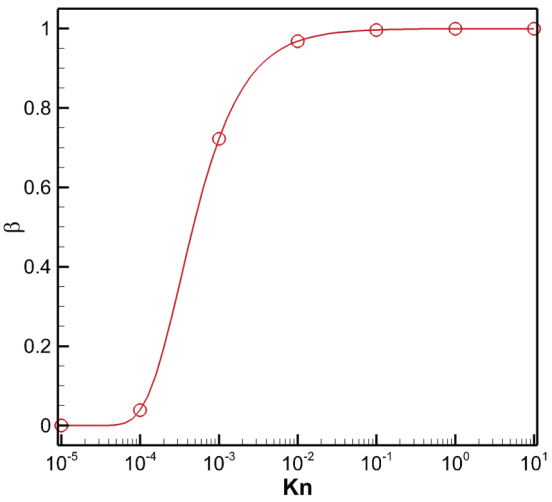

FIG. 2. Adaptive parameter vs Knudsen number for Sod shock tube problem.

where

$$\begin{aligned}\Delta\mathbf{F}_{c,j}^{n+1} &= \mathbf{F}_c\left(\mathbf{W}_j^n + \Delta\mathbf{W}_j^{n+1}\right) - \mathbf{F}_c\left(\mathbf{W}_j^n\right), \\ r_{ij} &= (|\mathbf{n}_{ij}\cdot\mathbf{u}_{ij}| + c_s) + \max\left(\frac{4}{3\rho_{ij}}, \frac{\gamma}{\rho_{ij}}\right)\frac{\mu_{ij}}{\mathrm{Pr}|\mathbf{d}_{ij}|}, \\ |\mathbf{d}_{ij}| &= |\mathbf{x}_j - \mathbf{x}_i|, \end{aligned}$$

and $\mathbf{F}_c = [\rho\mathbf{u}, \rho\mathbf{u}\mathbf{u} + p\mathbf{I}, (\rho E + p)\mathbf{u}]^T$ is the convective flux of the macroscopic governing equation; μ is the dynamic viscosity. Eq. (41) can be solved by two steps: the forward sweep and the backward sweep, i.e.,

$$\begin{aligned}&\left(\frac{V_i}{\Delta t_i} + \frac{1}{2}\sum_{j\in N(i)} r_{ij}S_{ij}\right)\overline{\Delta\mathbf{W}}_i^{n+1} \\ &\quad + \frac{1}{2}\sum_{j\in L(i)}\left[\mathbf{n}_{ij}\cdot\Delta\mathbf{F}_{c,j}^{n+1} - r_{ij}\overline{\Delta\mathbf{W}}_j^{n+1}\right]S_{ij} = -\mathbf{R}_i^n, \end{aligned} \tag{42}$$

$$\begin{aligned}&\left(\frac{V_i}{\Delta t_i} + \frac{1}{2}\sum_{j\in N(i)} r_{ij}S_{ij}\right)\Delta\mathbf{W}_i^{n+1} \\ &\quad + \frac{1}{2}\sum_{j\in U(i)}\left[\mathbf{n}_{ij}\cdot\Delta\mathbf{F}_{c,j}^{n+1} - r_{ij}\Delta\mathbf{W}_j^{n+1}\right]S_{ij} \\ &= \left(\frac{V_i}{\Delta t_i} + \frac{1}{2}\sum_{j\in N(i)} r_{ij}S_{ij}\right)\overline{\Delta\mathbf{W}}_i^{n+1}, \end{aligned} \tag{43}$$

where $L(i)$ and $U(i)$ are the subsets of $N(i)$; $L(i)$ denotes the neighboring cells of cell i occupying the lower triangular area of the matrix $\mathbf{A}_w$, and $U(i)$ represents the ones in the upper triangular area. Once the solution correction $\Delta\mathbf{W}_i^{n+1}$ is obtained, the predicted conservative variables at the cell center can be calculated by $\overline{\mathbf{W}}_i^{n+1} = \mathbf{W}_i^n + \Delta\mathbf{W}_i^{n+1}$.

We would like to reaffirm that in the improved implicit DVM, the particle collision effect is only considered in the evaluation of the macroscopic numerical flux in the prediction step. The evaluation of the microscopic numerical flux in

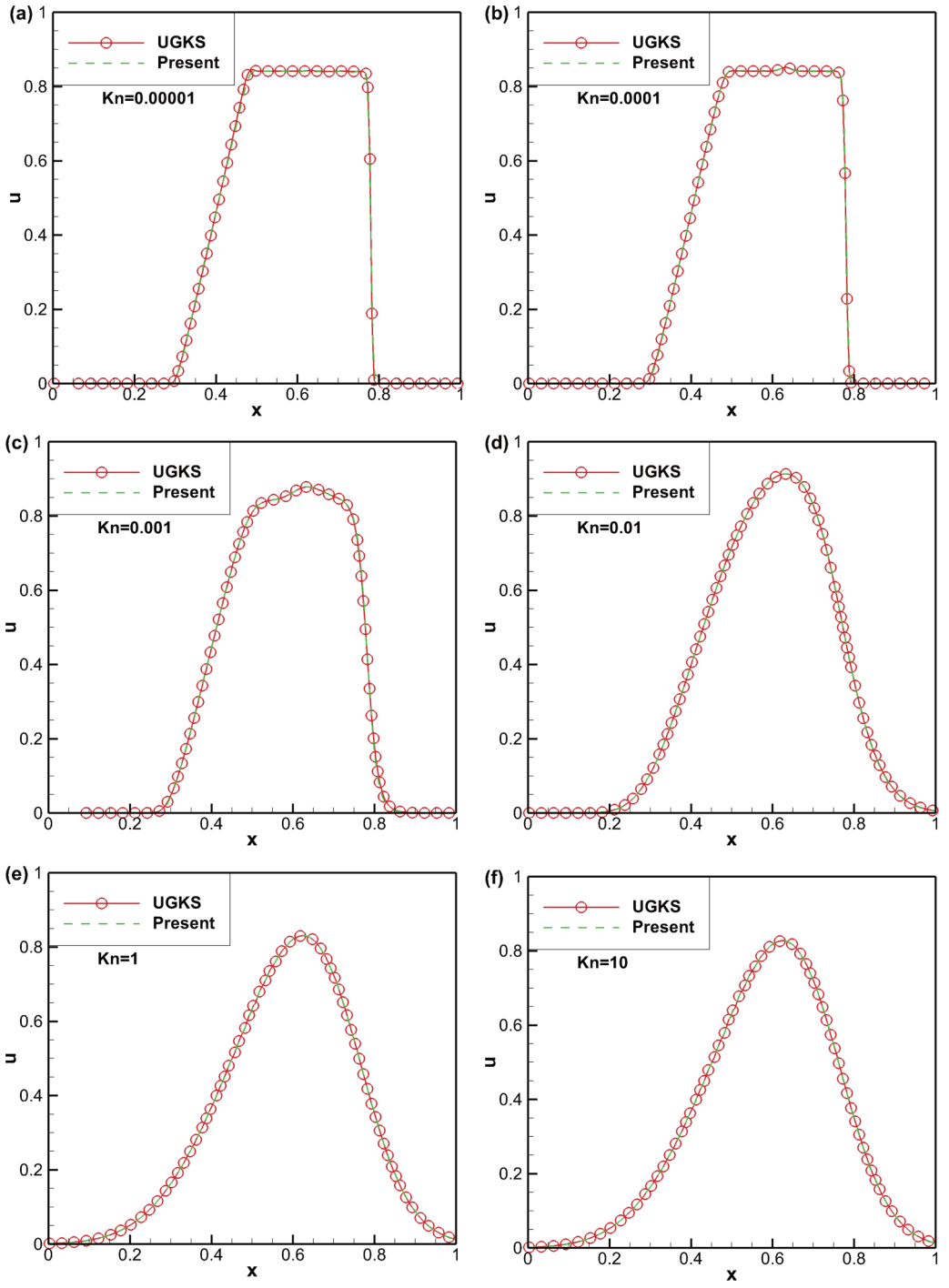

FIG. 3. Velocity profile of Sod shock tube problem at different Knudsen numbers. (a) Kn = 0.00001; (b) Kn = 0.0001; (c) Kn = 0.001; (d) Kn = 0.01; (e) Kn = 1; (f) Kn = 10.

DVBE follows the same way as the conventional DVM, which ignores the collision effect. Such distinct treatments of the macroscopic and the microscopic numerical fluxes have been validated numerically in the simplified UGKS of Chen *et al.* [34] and in the work of Yang *et al.* [33]. As shown in their work, the simplified approximation of the microscopic numerical flux has little influence on the overall accuracy. The possible explanation is that the evolution of the distribution function mainly affects the solutions of rarefied flows, while in the continuum flow regime, the macroscopic evolution in the prediction step dominates the solutions [33]. Correspondingly, the compromise in the accuracy of reconstructing microscopic numerical flux does not deteriorate the overall accuracy, but will significantly improve the computational efficiency. It is thus expected that the developed method can give accurate and efficient solutions over the whole flow regimes.

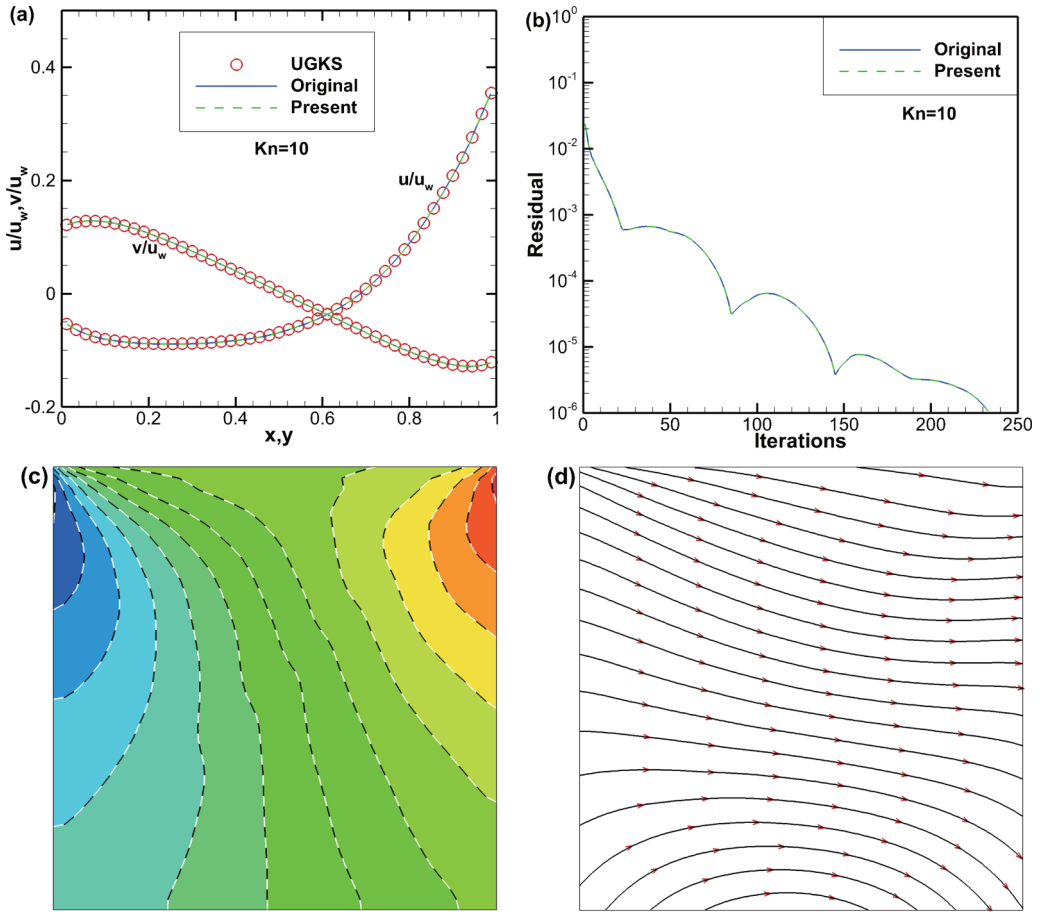

FIG. 4. Lid-driven cavity flow at Kn = 10. (a) Velocity profiles along the central lines. (b) Convergence history. (c) Temperature contours (Original: colored background with black solid line; Present: white dashed line). (d) Streamlines of heat flux (Original: black line; Present: red line with arrowhead).

B. Comparative analysis with simplified UGKS

In the work of Chen *et al.* [34], three simplified UGKS were presented to improve computational efficiency and reduce the complexity of the original UGKS. Among these simplified UGKS, the second version also computes the microscopic numerical flux by the collisionless solution of the Boltzmann equation and evaluates the macroscopic numerical flux by simply combining the flux attributed to the collisionless solution of the Boltzmann equation and that of the Navier-Stokes equations. To clearly show the differences between the second simplified UGKS and the present method, a brief comparison is given in this section.

As shown in the work of Chen *et al.* [34], the numerical fluxes at the cell interface of the second simplified UGKS can be written as

$$\mathbf{F}^{\alpha}_{S2} = \boldsymbol{\xi}_{\alpha}\left(\Delta t_p f_{\alpha} - \frac{1}{2}\Delta t_p^2 \boldsymbol{\xi}_{\alpha}\cdot\nabla f_{\alpha}\right), \tag{44}$$

$$\begin{aligned}\mathbf{F}^{w}_{S2} = {} & \beta\left\langle \boldsymbol{\xi}\boldsymbol{\psi}\left(\Delta t_p f - \frac{1}{2}\Delta t_p^2 \boldsymbol{\xi}\cdot\nabla f\right)\right\rangle_{\alpha} \\ & + (1-\beta)\left\langle \boldsymbol{\xi}\boldsymbol{\psi}\left[\Delta t_p f^{\mathrm{eq}} - \Delta t_p \tau\left(\boldsymbol{\xi}\cdot\nabla f^{\mathrm{eq}} + \frac{\partial f^{\mathrm{eq}}}{\partial t}\right)\right.\right. \\ & \left.\left. + \frac{1}{2}\Delta t_p^2 \frac{\partial f^{\mathrm{eq}}}{\partial t}\right]\right\rangle,\end{aligned} \tag{45}$$

where $\mathbf{F}^{\alpha}_{S2}$ and $\mathbf{F}^{w}_{S2}$ are, respectively, the microscopic and macroscopic numerical fluxes. $f_{\alpha} = f_{\mathrm{DVM}}(\mathbf{x}_{ij}, \boldsymbol{\xi}_{\alpha}, \Delta t_p)$ is the distribution function at the cell interface given by Eq. (21). f^{eq} is the equilibrium state at the cell interface. The symbol $\langle f\rangle$ is defined as $\langle f\rangle = \int_{-\infty}^{+\infty} f d\mathrm{E}$. Note that the integral over time interval Δt_p has been carried out in evaluating the numerical fluxes of the second simplified UGKS.

In the present method, the microscopic and macroscopic numerical fluxes at the cell interface integrated over time interval Δt_p can be summarized as follows:

$$\mathbf{F}^{\alpha}_{\mathrm{Current}} = \boldsymbol{\xi}_{\alpha}\Delta t_p f_{\alpha}, \tag{46}$$

$$\mathbf{F}^{w}_{\mathrm{Current}} = \beta\langle \boldsymbol{\xi}\boldsymbol{\psi}\Delta t_p f\rangle_{\alpha} + (1-\beta)\langle \boldsymbol{\xi}\boldsymbol{\psi}\Delta t_p f_{\mathrm{NS}}\rangle. \tag{47}$$

In Eq. (47), the last term is actually the numerical flux of the Navier-Stokes equations. According to the kinetic theory [25], we have $f_{\mathrm{NS}} = f^{\mathrm{eq}} - \tau D f^{\mathrm{eq}} + O(\tau^2)$. As a result, Eq. (47) can be rewritten as

$$\begin{aligned}\mathbf{F}^{w}_{\mathrm{Current}} = {} & \beta\langle \boldsymbol{\xi}\boldsymbol{\psi}\Delta t_p f\rangle_{\alpha} + (1-\beta)\left\langle \boldsymbol{\xi}\boldsymbol{\psi}\left[\Delta t_p f^{\mathrm{eq}}\right.\right. \\ & \left.\left. - \Delta t_p \tau\left(\boldsymbol{\xi}\cdot\nabla f^{\mathrm{eq}} + \frac{\partial f^{\mathrm{eq}}}{\partial t}\right)\right]\right\rangle.\end{aligned} \tag{48}$$

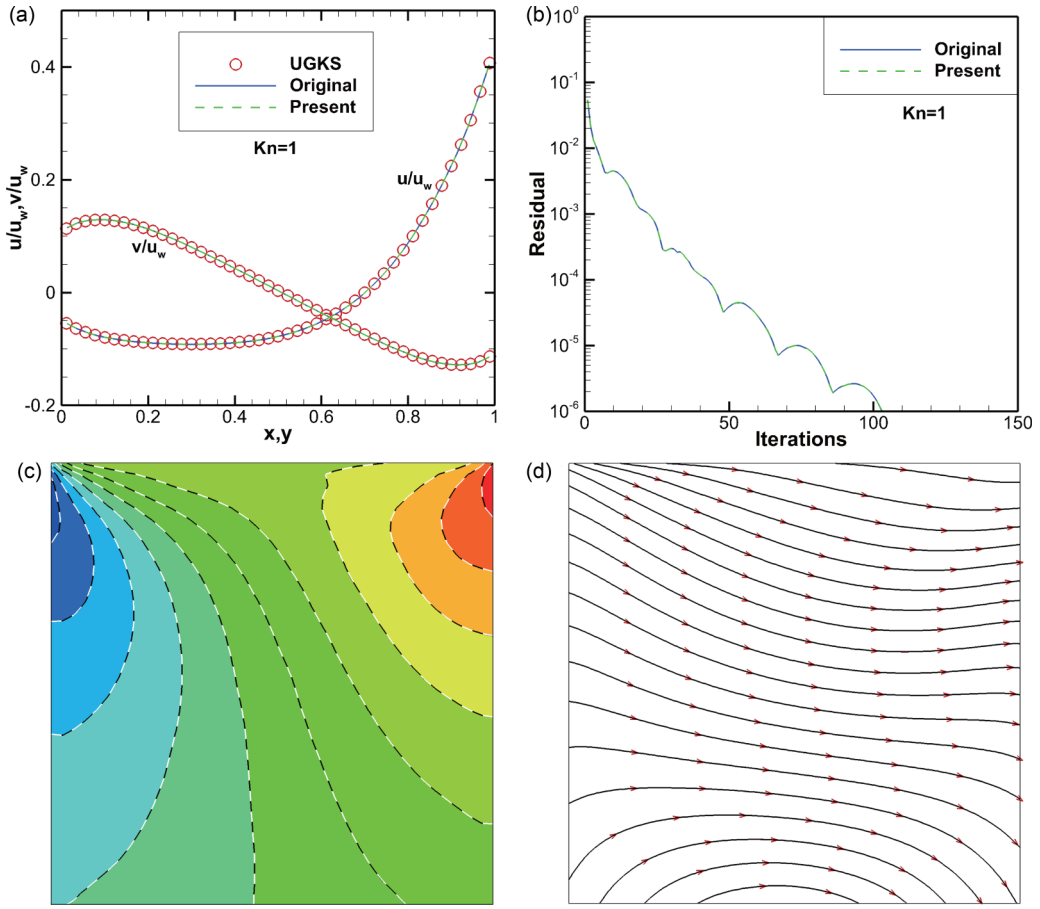

FIG. 5. Lid-driven cavity flow at Kn = 1. The caption is the same as in Fig. 4.

By comparing Eq. (44) with Eq. (46), it can be seen that the microscopic numerical flux in the second simplified UGKS is computed by the collisionless solution of the Boltzmann equation with a piecewise linear distribution for the distribution function at the cell interface, while a piecewise constant distribution is utilized in the present method. A similar way is also used in the calculation of the macroscopic numerical flux attributed to the collisionless solution of the Boltzmann equation, as shown in the first term on the right-hand side of Eq. (45) and Eq. (48). The use of the collisionless solution of the Boltzmann equation with a piecewise linear distribution may introduce a large numerical dissipation into the solution. This speculation will be shown in the numerical examples presented in Sec. V.

In addition, the macroscopic numerical flux of these two schemes in the continuum flow regime is somewhat different. Assume that the initial distribution function at the beginning of the time step satisfies the near-equilibrium state, i.e.,

$$f = f^{\mathrm{eq}} - \tau\left(\boldsymbol{\xi}\cdot\nabla f^{\mathrm{eq}} + \frac{\partial f^{\mathrm{eq}}}{\partial t}\right). \tag{49}$$

Substituting Eq. (49) into Eq. (45), the macroscopic numerical flux of the second simplified UGKS becomes

$$\mathbf{F}^{w}_{S2} = \left\langle \boldsymbol{\xi}\boldsymbol{\psi}\left[\Delta t_p f^{\mathrm{eq}} - \Delta t_p \tau\left(1-\frac{\Delta t_p}{2\tau}\beta\right)\left(\boldsymbol{\xi}\cdot\nabla f^{\mathrm{eq}} + \frac{\partial f^{\mathrm{eq}}}{\partial t}\right) + \frac{1}{2}\Delta t_p^2 \frac{\partial f^{\mathrm{eq}}}{\partial t}\right]\right\rangle. \tag{50}$$

And substituting Eq. (49) into Eq. (48), the macroscopic numerical flux of the present method can be written as

$$\mathbf{F}^{w}_{\mathrm{Current}} = \left\langle \boldsymbol{\xi}\boldsymbol{\psi}\left[\Delta t_p f^{\mathrm{eq}} - \Delta t_p \tau\left(\boldsymbol{\xi}\cdot\nabla f^{\mathrm{eq}} + \frac{\partial f^{\mathrm{eq}}}{\partial t}\right)\right]\right\rangle. \tag{51}$$

It can be seen that the viscosity of the second simplified UGKS is enlarged by a factor of $1-\beta\Delta t_p/(2\tau)$, while the present scheme provides the accurate macroscopic numerical flux in the continuum limit. Besides that, the present scheme computes the macroscopic numerical flux attributed to the Navier-Stokes equations directly by the commonly used Roe scheme and the central difference scheme [35,41], while the second simplified UGKS evaluates this portion of flux by the gas kinetic scheme for continuum flows.

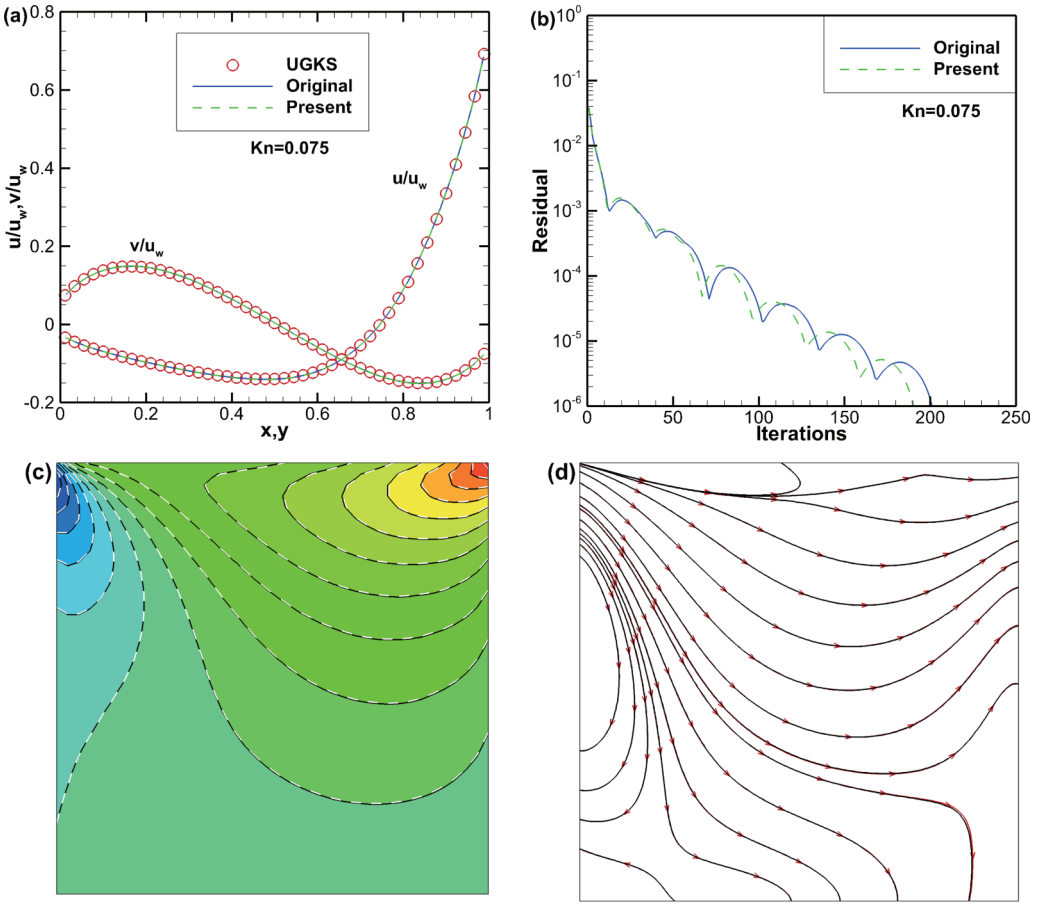

FIG. 6. Lid-driven cavity flow at Kn = 0.075. The caption is the same as in Fig. 4.

C. Boundary conditions and computational sequence

Since the proposed method involves the microscopic and the macroscopic evolutions, proper boundary conditions of both the distribution function and the conservative variables are needed. For the boundary condition of the distribution function, which is related to the evaluation of the microscopic residual $\overline{\mathrm{Res}}^n_{i,\alpha}$ and the numerical flux $\mathbf{F}^{w,n}_{ij,DVM}$ at the boundary, it can be given in the same way as the conventional DVM [10,33]. As for the boundary condition of the conservative variables, it is only used for the calculation of macroscopic numerical flux $\mathbf{F}^{w,n}_{ij,NS}$. Thus, similar boundary treatments of macroscopic variables in the conventional Navier-Stokes solvers can be utilized [41].

The basic solution procedure of the improved implicit DVM is summarized as follows:

(1) Reconstruct the distribution function at the cell interface $f_{\mathrm{DVM}}(\mathbf{x}_{ij}, \boldsymbol{\xi}, \Delta t_p)$ by the collisionless solution of the Boltzmann equation [Eq. (21)].

(2) Compute $\mathbf{F}^{w,n}_{ij,NS}$ by the conventional Navier-Stokes solver and $\mathbf{F}^{w,n}_{ij,DVM}$ by Eq. (37).

(3) Calculate the physical time step Δt_p by Eq. (20), the collision time scale τ by Eq. (53), and the adaptive parameter β by Eq. (38).

(4) Compute the total macroscopic numerical flux $\mathbf{F}^{w}_{ij}$ by Eq. (37), the macroscopic residual $\mathbf{R}^n_i$ by Eq. (40), and the time step for implicit iteration Δt by Eq. (9).

TABLE I. Iteration step and computational time (hours) of different methods for lid-driven cavity flow at different Knudsen and Reynolds numbers.

	Original		Present		Speedup	
Kn or Re	Step (S_O)	Time (T_O)	Step (S_I)	Time (T_I)	S_O/S_I	T_O/T_I
Kn = 10	233	0.366	233	0.372	1.000	0.984
Kn = 1	102	0.161	102	0.164	1.000	0.982
Kn = 0.075	201	0.033	190	0.032	1.058	1.031
Re = 100	19158	1.550	4937	0.417	3.880	3.717
Re = 1000	412358	33.680	11048	0.938	37.324	35.906

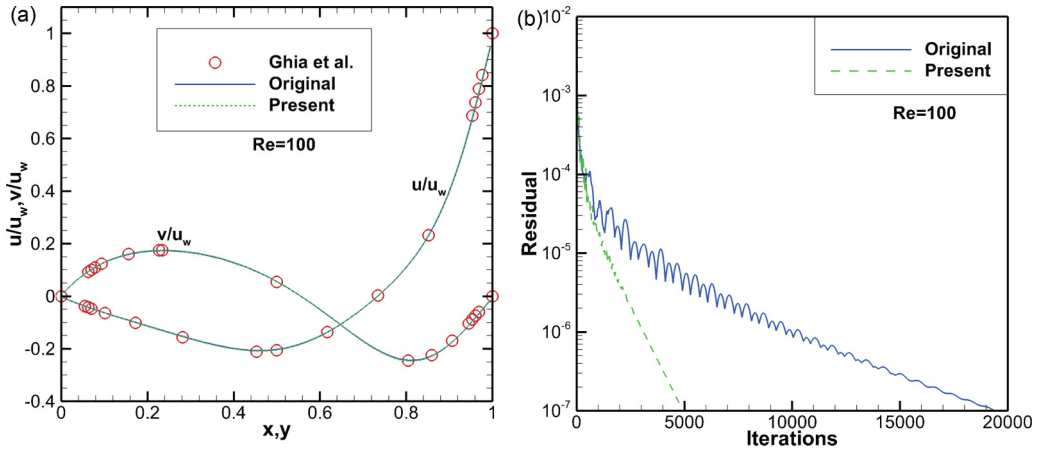

FIG. 7. Lid-driven cavity flow at Re = 100. (a) Velocity profiles along the central lines. (b) Convergence history.

(5) Solve the macroscopic governing equation by the forward sweep of Eq. (42) and the backward sweep of Eq. (43). This step gives the predicted conservative variables at the new time step $\overline{\mathbf{W}}_i^{n+1}$.

(6) Compute the predicted equilibrium state $\overline{f}_\alpha^{\mathrm{eq},n+1}$ by substituting $\overline{\mathbf{W}}_i^{n+1}$ into Eqs. (2) and (3). In this step, the heat flux is approximated by its value at last time step $\mathbf{q}^n$.

(7) Calculate the microscopic residual $\overline{\mathrm{Res}}_{i,\alpha}^n$ by Eq. (24) and solve the microscopic governing equation by LU-SGS method. This step gives the distribution function at the new time step $f_{i,\alpha}^{n+1}$.

(8) Update the conservative variables, heat flux and stress tensor by Eqs. (4)–(6).

(9) Repeat steps (1) to (8) until the convergence criterion is satisfied.

V. NUMERICAL EXAMPLES

In this section, the Sod shock tube problem, the lid-driven cavity flow, and the flat plate flow from the free molecular regime to the continuum regime and the hypersonic rarefied flow over a cylinder are simulated for the comprehensive evaluation of the improved fully implicit DVM. Special attention will be paid to the comparative study with the conventional semi-implicit DVM in terms of accuracy and efficiency. In practical calculations, all flow variables are normalized following the strategy in Ref. [7]. In the simulations, the Prandtl number is taken as Pr = 2/3, and the CFL number for calculation of the physical time step is set as $\sigma_p = 0.95$. Unless otherwise stated, the CFL number for implicit discretization is chosen as $\sigma = 100$. All the computations were carried out on a PC with a processor of Intel(R) Xeon(R) E5-2687 CPU@3.0 GHz, and no parallel technique is adopted. For convenience, the results of the conventional semi-implicit DVM and the present scheme are denoted as "Original" and "Present," respectively.

A. Case 1: Sod shock tube problem

At first, the one-dimensional Sod shock tube problem is tested under a wide range of Knudsen numbers to validate the performance of the improved DVM. The initial condition of this problem is given by

$$\begin{aligned}(\rho_1, u_1, p_1) &= (1, 0, 1), \quad 0 < x < 0.5,\\ (\rho_2, u_2, p_2) &= (0.125, 0, 0.1), \quad 0.5 < x < 1.\end{aligned} \tag{52}$$

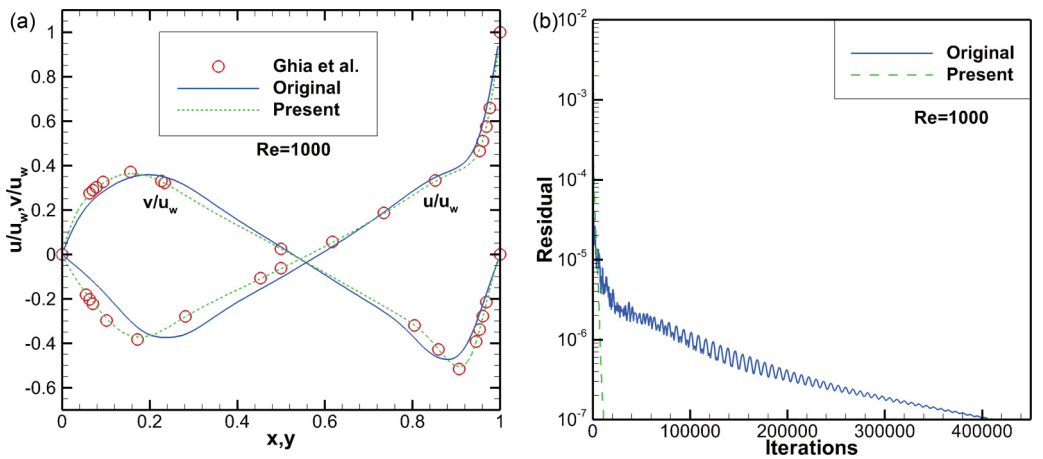

FIG. 8. Lid-driven cavity flow at Re = 1000. (a) Velocity profiles along the central lines. (b) Convergence history.

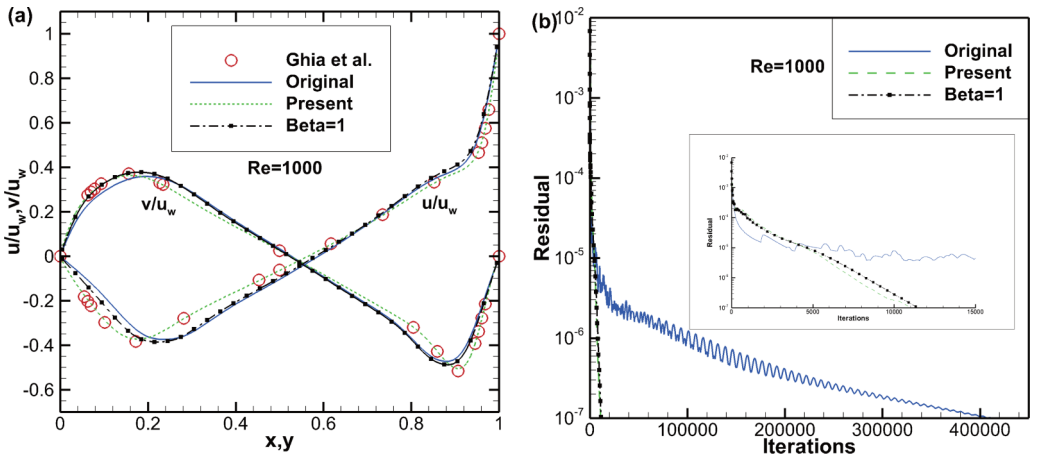

FIG. 9. Simulation results of lid-driven cavity flow at Re = 1000 obtained by different methods. (a) Velocity profiles along the central lines. (b) Convergence history.

The collision timescale and the dynamic viscosity are, respectively, computed by

$$\tau = \mu/p, \tag{53}$$

$$\mu = \mu_{\text{ref}}(T/T_{\text{ref}})^{w}, \tag{54}$$

where μ_{ref}, T_{ref}, and w are the reference viscosity, the reference temperature, and the coefficient related to the intermolecular interaction model, respectively. In this test, the hard-sphere (HS) model is utilized, which gives $w = 0.5$. The reference viscosity is related to the Knudsen number by

$$\text{Kn} = \frac{\mu_{\text{ref}}\sqrt{RT_{\text{ref}}}}{p_{\text{ref}}L}, \tag{55}$$

where p_{ref} is the reference pressure and $L = 1$ is the characteristic length. In the simulation, (ρ_1, u_1, p_1) are taken as the reference state. Consistent with previous study [34], in the present work, the computational domain is divided uniformly into 200 cells. In the particle velocity space, 150 points with uniform distribution in $[-6, 6]$ are used and the Newton-Cotes quadrature is utilized for integration. Since it is an unsteady problem, the explicit temporal discretization is adopted in this case for simplicity and the CFL number is taken as $\sigma = 0.9$.

In the simulation, the Knudsen number is varied from 10^{-5} to 10. The adaptive parameter β in Eq. (38) computed by the reference state is depicted in Fig. 2. It can be seen that the value of β changes from 0 to 1 for the Knudsen numbers considered in our simulation, which can be used to investigate the effect of β on the performance of the present method from the continuum flow regime to the rarefied flow regime. Figure 3 shows the velocity profiles at different Knudsen numbers computed by the present scheme and the original UGKS [24] at time $t = 0.15$. As expected, the improved DVM provides very good results for all cases, which validates the accuracy of the present scheme for flows over all Knudsen numbers. However, for the cases of Kn = 1 and 10, a discrepancy between the result of the second simplified UGKS and that of the original UGKS was reported by Chen *et al.* [34].

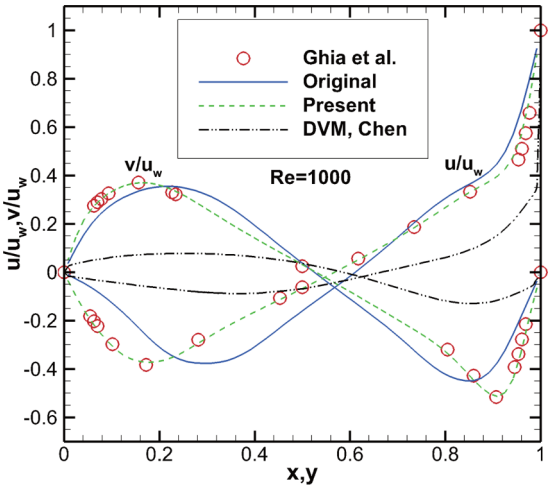

FIG. 10. Velocity profiles along the central lines for lid-driven cavity flow at Re = 1000 computed by different methods with mesh size of 60 × 60 cells.

B. Case 2: Lid-driven cavity flow

The lid-driven cavity flow with different Knudsen numbers or Reynolds numbers is simulated in this section. In this test example, the monatomic gas is considered, i.e., $N = 0$. As a result, the specific heat ratio γ is equal to 5/3.

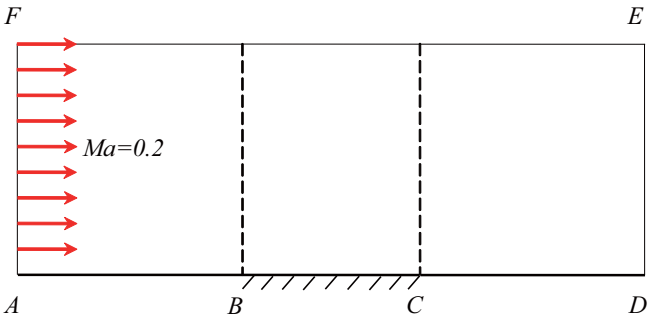

FIG. 11. Illustration of the computational domain for flat plate flow.

TABLE II. Discretization in physical space for flat plate flow. N_{BC} is the numbers of discrete cells on edge BC. N_{AF} is the numbers of discrete cells on edge AF, which equal to those on edges AB and CD, i.e., $N_{\mathrm{AF}} = N_{\mathrm{AB}} = N_{\mathrm{CD}}$. $\delta x_{\min}$ denotes the minimum width of cells near points B and C. $\delta y_{\min}$ denotes the minimum height of cells near the bottom boundary.

Re	N_{BC}	N_{AF}	N_{total}	$\delta x_{\min}$	$\delta y_{\min}$
0.2	32	32	3072	1/32	0.02
0.5, 1	48	48	6912	1/48	0.01
2, 5	48	48	6912	0.01	0.005
10, 20, 50	64	48	7680	0.005	0.002
400	80	48	8448	0.001	0.001
1000, 2000	96	48	9216	0.0005	0.0005
5000	112	48	9984	0.0002	0.0002

The computational domain is a square cavity with the edge length of $L = 1$. At the top boundary, the normalized wall temperature and velocity are fixed at $T_W = 1$ and $u_W = 0.15$, respectively. The other walls are stationary and are assigned with constant temperature of $T_W = 1$. The collision timescale and the dynamic viscosity are also computed by Eq. (53) and Eq. (54), while the reference temperature T_{ref} is replaced by T_W and the variable hard-sphere (VHS) model is utilized, which gives $w = 0.81$. For the rarefied case, the reference viscosity is determined by

$$\frac{\mu_{\mathrm{ref}}}{L} = \frac{5\rho_0(2\pi RT_0)^{1/2}}{16}\mathrm{Kn}. \tag{56}$$

Here, $\rho_0 = 1$ and $T_0 = T_W$ are, respectively, the normalized density and temperature at the reference state. After normalization, the gas constant is $R = 0.5$. For the continuous case, the reference viscosity is calculated by

$$\mu_{\mathrm{ref}} = \frac{\rho_0 u_W L}{\mathrm{Re}}, \tag{57}$$

where Re is the Reynolds number. The convergence criteria for the rarefied and the continuous cases are set by the condition that the maximum errors of all primitive variables between two adjacent iteration steps do not exceed 10^{-6} and 10^{-7}, respectively.

First, three cases with different Knudsen numbers of Kn = 10, 1, and 0.075 are simulated. These three cases, respectively, correspond to the free molecular flow regime ($\mathrm{Kn} \geqslant 10$), transition flow regime ($10^{-1} \leqslant \mathrm{Kn} < 10$), and slip flow regime ($10^{-2} \leqslant \mathrm{Kn} < 10^{-1}$). In the simulation, the computational domain is divided uniformly into 40×40 cells. In the particle velocity space, the Newton-Cotes quadrature with 81×81 mesh points uniformly distributed in $[-4, 4] \times [-4, 4]$ is utilized in the cases of Kn = 10 and 1, and the Gauss-Hermite quadrature with 28×28 mesh points is used in the case of Kn = 0.075. Specifically, the CFL number for implicit discretization in the case of Kn = 10 is taken as $\sigma = 10$ to ensure convergence. Simulation results are shown in Figs. 4–6. The present improved implicit DVM and the conventional semi-implicit DVM give similar solutions on velocity profiles, temperature contours, and streamlines of heat flux; and good agreements with the results of UGKS [24] are achieved by both methods. As shown in the plots of convergence history, the present scheme shows a comparable convergence rate as the conventional semi-implicit DVM at Kn = 10 and 1, and converges faster than the conventional one in the case of Kn = 0.075. This observation can also be validated by the quantities in Table I. Little extra computational time is consumed by the present method in the first two cases of Kn = 10 and 1 due to additional efforts in the prediction step, while the present method shows higher efficiency in the case of Kn = 0.075. The speed-up in the last case is attributed to the effectiveness of the prediction step since the flow is approaching to the continuum flow regime. In this case, the adaptive parameter in Eq. (38) reads $\beta = 0.978$. As a result, the prediction step is beginning to take effect on the solutions.

To further investigate the performance of the developed fully implicit DVM in the continuum flow regime, two more cases at Reynolds numbers of Re = 100 and 1000 are simulated. The corresponding Knudsen numbers are Kn = 0.00271 and 0.000271. In the simulations, the computational domain is discretized by 100×100 uniform cells, while the integration over the particle velocity space is accomplished by the Gauss-Hermite quadrature with 8×8 mesh points. Figures 7 and 8 show the velocity distributions along the center lines and the convergence histories of the lid-driven

TABLE III. Iteration step and computational time (hours) of different methods for flat plate flow at different Reynolds numbers.

		Original		Present		Speedup	
Re	Kn	Step (S_O)	Time (T_O)	Step (S_I)	Time (T_I)	S_O/S_I	T_O/T_I
0.2	1.19	241	0.076	222	0.073	1.086	1.041
0.5	0.476	477	0.350	387	0.288	1.233	1.215
1	0.238	821	0.621	609	0.466	1.348	1.333
2	0.119	1258	0.936	902	0.678	1.395	1.381
5	0.0476	2655	1.957	1558	1.163	1.704	1.683
10	0.0238	4876	4.085	2164	1.842	2.253	2.218
20	0.0119	8906	7.478	3070	2.637	2.901	2.836
50	0.00476	19087	16.183	4654	3.982	4.101	4.064
400	0.000595	39776	37.403	8917	8.512	4.461	4.394
1000	0.000238	46081	48.213	11627	12.417	3.963	3.883
2000	0.000119	44593	47.064	13174	14.037	3.385	3.353
5000	0.0000476	42731	51.352	15485	18.662	2.760	2.752

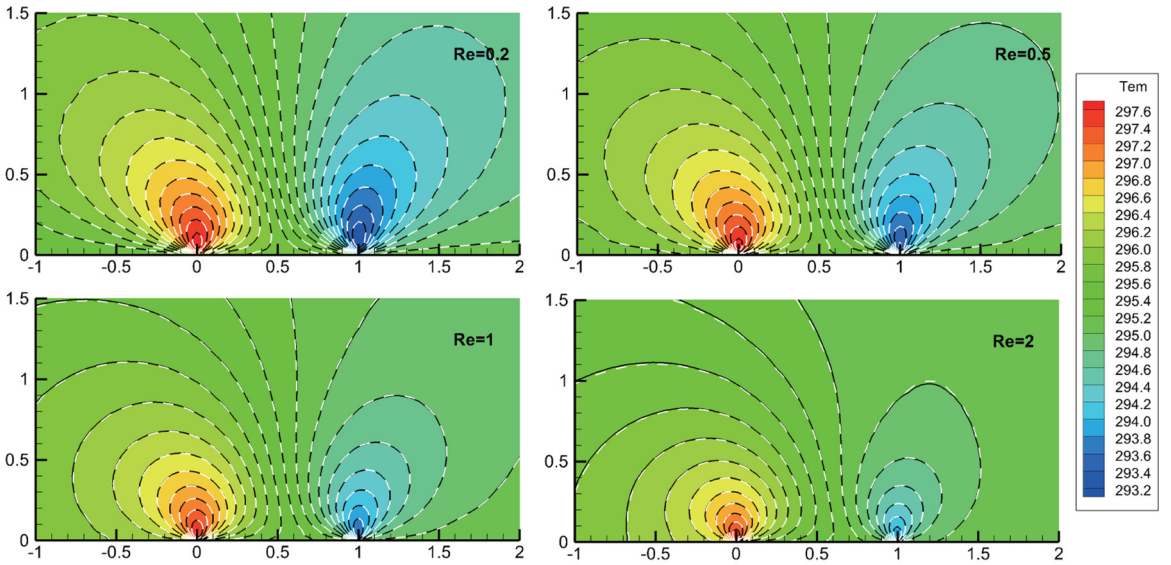

(a) *Re*=0.2~2

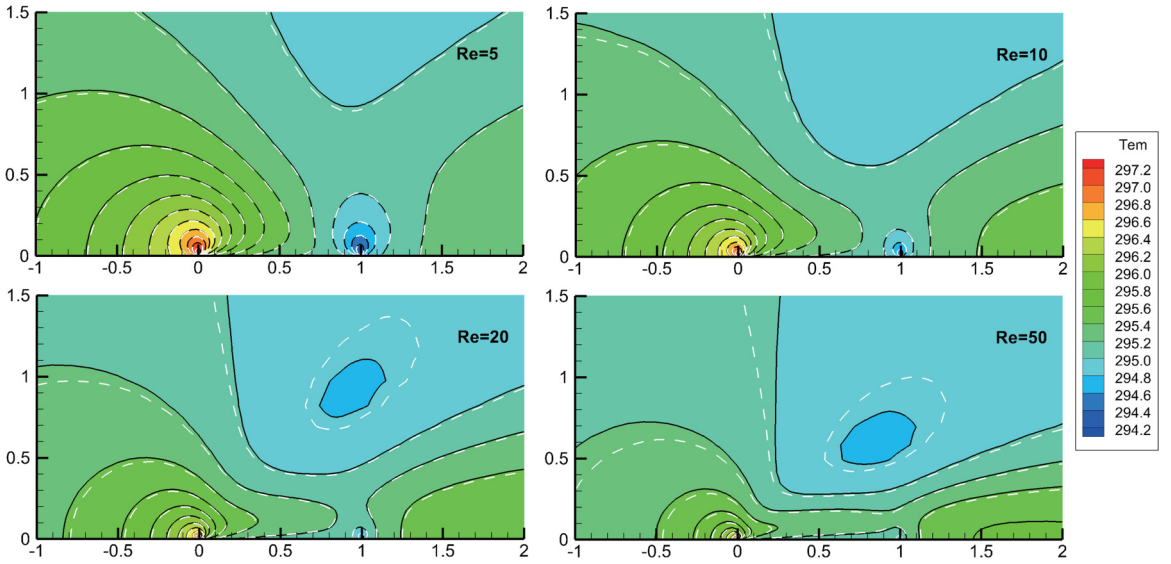

(b) *Re*=5~50

FIG. 12. Temperature contours around the flat plate in the transition and the slip flow regimes (Original: colored background with black solid line; Present: white dashed line).

cavity flow at Re = 100 and 1000, respectively. In the case of Re = 100, both the present method and the original model give accurate prediction of the velocity profiles [44], which is due to the fact that the cell size is of the order of the mean free path ($\lambda/\Delta x = 0.271$). In the case of Re = 1000, however, the results of the present method are far better than the original one. As analyzed above, this improvement comes from the introduced prediction step with the particle collision effect,

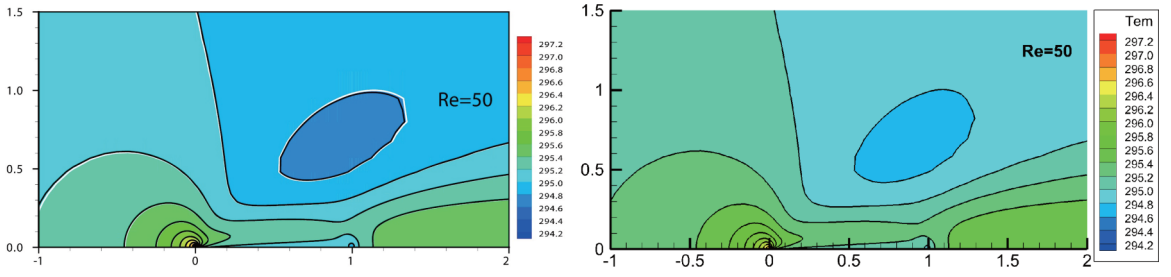

FIG. 13. Temperature contours around the flat plate at Re = 50 (Left: UGKS [49]; Right: Present).

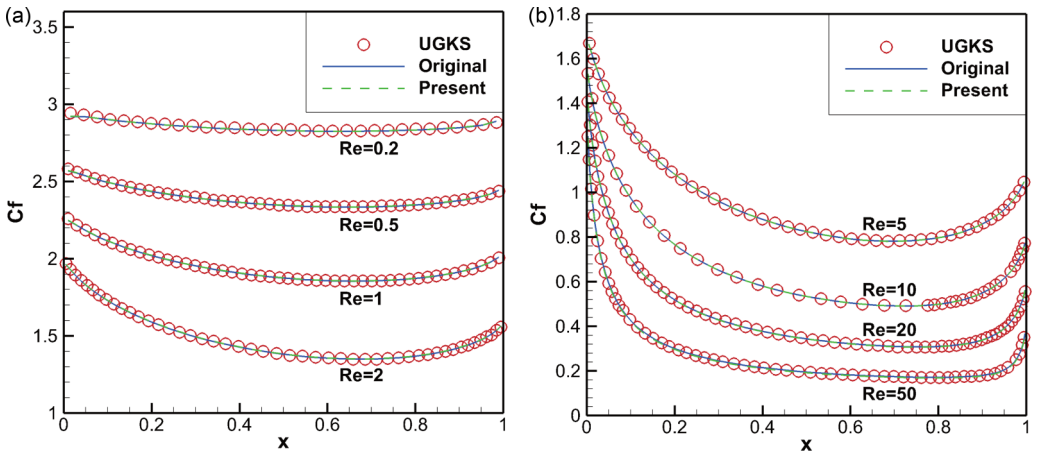

FIG. 14. Distribution of the skin friction coefficient on the flat plate in the transition and the slip flow regimes. (a) Re = 0.2 ∼ 2; (b) Re = 5 ∼ 50.

which plays an essential role in the continuum flow regime. The ratio of the mean free path to the cell size here reads $\lambda/\Delta x = 0.0271$, which means that the conventional semi-implicit DVM would require much finer mesh size to make up its defect of ignoring collision effects in reconstructing numerical fluxes. Specifically, the adaptive parameter β has the values of $\beta = 0.607$ and $\beta = 0.00683$ in the cases of Re = 100 and 1000, respectively. The tendency of β approaching zero physically represents the increased importance of the particle collision effect, and numerically corresponds to a larger portion from the Navier-Stokes solver when reconstructing numerical fluxes in the improved implicit DVM. Another notable issue is that the computational efficiency in the continuum flow regime is significantly improved by adopting this method. A higher convergence rate is observed in our simulations [see Figs. 7(b) and 8(b)]. As reported in Table I, the speed-up rates of the present method are around 3.7 and 36 in the cases of Re = 100 and 1000, respectively.

Next, we simulate the case of Re = 1000 by using the improved scheme with a fixed value of $\beta = 1$ in Eq. (38). With such settings, the numerical flux in the macroscopic governing equation is reconstructed from the local solution of collisionless Boltzmann equation, which follows a similar strategy as the conventional semi-implicit DVM. It is shown in the modeling [see Fig. 9(a)] that ignoring the collision effect would deteriorate the results in the continuum flow regime and lead to similar velocity profiles as the conventional semi-implicit DVM. However, as presented in Fig. 9(b), the speed-up of the convergence rate can still be ensured even if the developed fully implicit DVM is assigned with fixed parameter of $\beta = 1$. This evidence demonstrates that introducing the prediction step could effectively increase the convergence rate for the simulation of flows in the continuum flow regime, while incorporating the collision effect into the evaluation of numerical fluxes leads to higher accuracy in this flow regime.

Finally, the case of Re = 1000 with a coarse mesh is simulated by the conventional semi-implicit DVM and the improved implicit DVM. Consistent with previous study [34], in our simulation, the computational domain is discretized by 60 × 60 uniform cells. Figure 10 compares the velocity profiles along the central lines obtained by the conventional semi-implicit DVM used in this work, the improved implicit DVM, and the conventional DVM shown in the work of Chen *et al.* [34]. The last method uses the collisionless solution of the Boltzmann equation with a piecewise linear distribution for the distribution function at the cell interface to reconstruct the numerical flux. It can be seen from this figure that the improved implicit DVM provides accurate velocity distribution with such coarse resolution, while the results of the conventional DVM used in both the current work and the work of Chen *et al.* [34] deviate significantly from the reference data [44]. On the other hand, as compared with the conventional DVM shown in the work of Chen *et al.* [34], the velocity profiles computed by the conventional semi-implicit DVM used in this work are closer to the benchmark data. It can then be inferred that the use of the collisionless solution of the Boltzmann equation with a piecewise linear distribution may produce a larger numerical dissipation than the piecewise constant distribution.

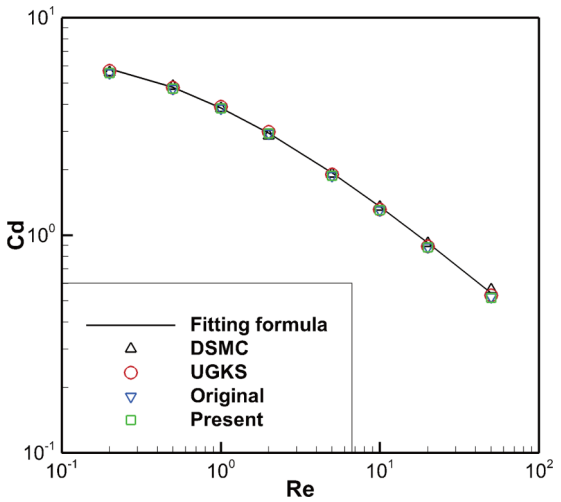

FIG. 15. Drag coefficient of the flat plate with respect to the Reynolds number in the transition and the slip flow regimes.

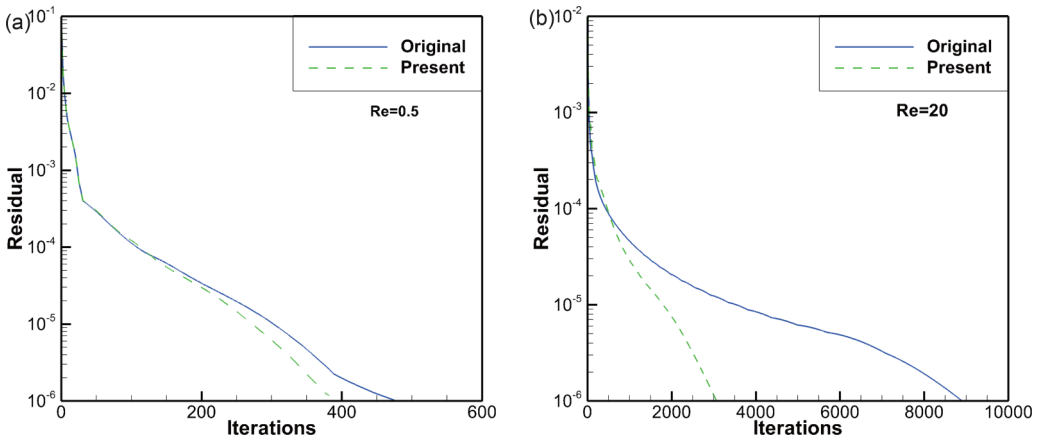

FIG. 16. Convergence history for flat plate flow in the transition and the slip flow regimes. (a) Transition flow regime at Re = 0.5. (b) Slip flow regime at Re = 20.

C. Case 3: Flat plate flow

The third test case is the subsonic flow over a flat plate with zero thickness at zero angle of attack [19,45–49]. In this case, the fluid substance is air, which gives $N = 2$ and the specific heat ratio is $\gamma = 7/5$. As shown in Fig. 11, the simulation mimics a flat plate with the length of $L_{\mathrm{BC}} = 1\,\mathrm{m}$ and temperature of $T_W = 295\,\mathrm{K}$ placed at the bottom boundary. The computation domain is truncated at $20L_{\mathrm{BC}}$ away from the leading and the trailing edges of the flat plate, i.e., $L_{\mathrm{AB}} = L_{\mathrm{CD}} = L_{\mathrm{AF}} = 20L_{\mathrm{BC}}$. The far field boundary condition is utilized for the left, the right, and the upper boundaries, while the symmetric boundary condition is implemented on the bottom boundary, except the flat plate which is treated as the isothermal wall boundary. The free stream temperature is taken as $T_\infty = 295\,\mathrm{K}$ and the Mach number is set to be

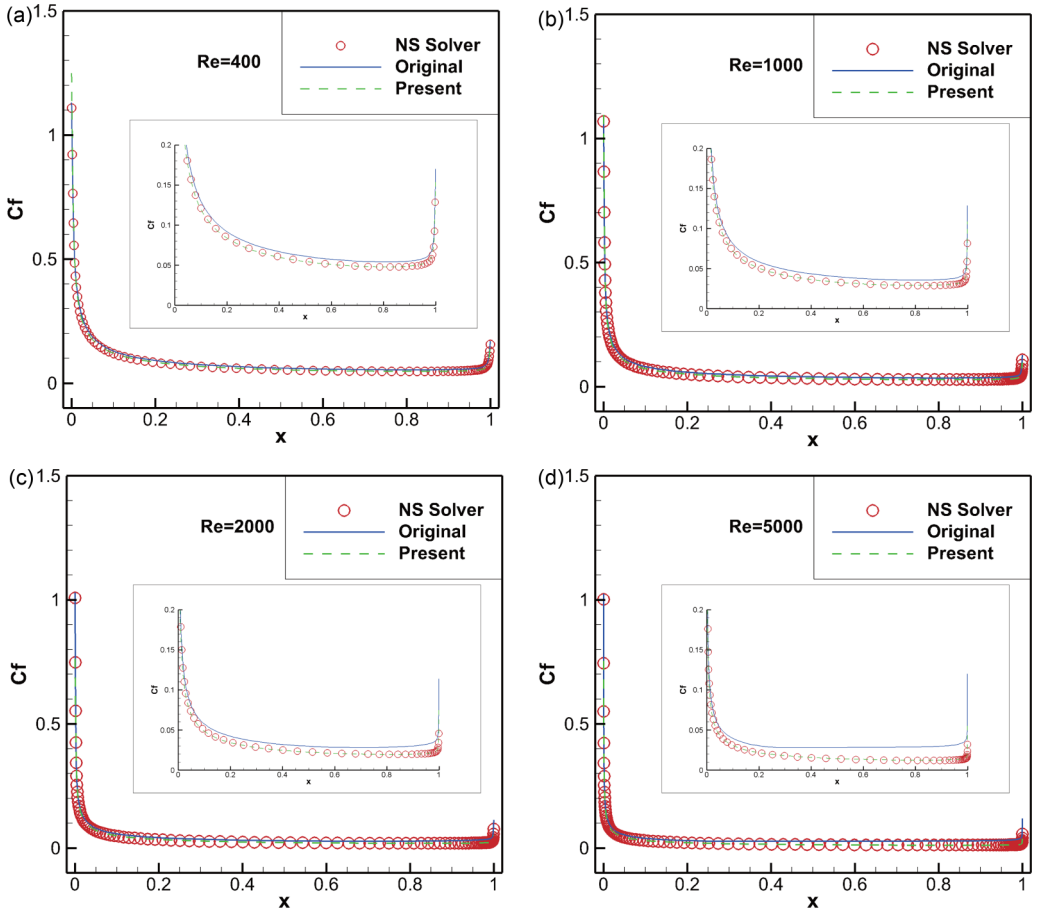

FIG. 17. Distribution of the skin friction coefficient on the flat plate in the continuum flow regime. (a) Re = 400; (b) Re = 1000; (c) Re = 2000; (d) Re = 5000.

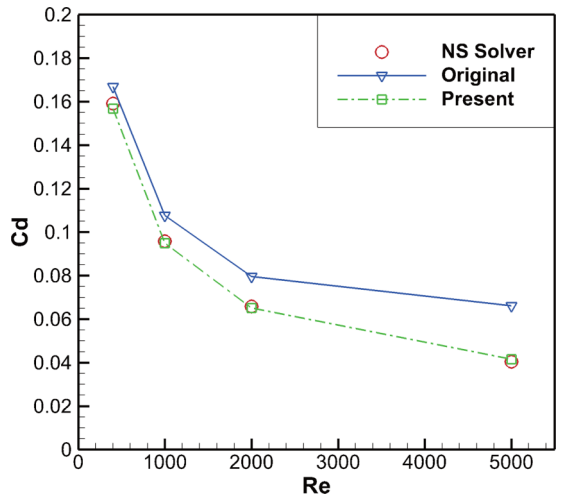

FIG. 18. Drag coefficient of the flat plate with respect to the Reynolds number in the continuum flow regime.

$\mathrm{Ma} = 0.2$. In the simulation, the dynamic viscosity μ is computed by Eq. (54) with $T_{\mathrm{ref}} = T_\infty$ and $w = 0.77$. After normalization, the reference viscosity can be determined by

$$\mu_{\mathrm{ref}} = \frac{\mathrm{Ma}}{\mathrm{Re}}\sqrt{\frac{\gamma}{2}}, \tag{58}$$

where Re is the Reynolds number defined with respect to the length of the plate. The global Knudsen number, Reynolds number, and Mach number have a relation of

$$\mathrm{Kn} = \frac{2(5-2w)(7-2w)}{15}\frac{\mathrm{Ma}}{\mathrm{Re}}\sqrt{\frac{\gamma}{2\pi}}. \tag{59}$$

The discretization in the physical space is listed in Table II for different Reynolds numbers. Note that the computational mesh is distributed nonuniformly and the local time step is utilized to speed up the convergence rate. In the particle velocity space, the Gauss-Hermite quadrature with 28×28 mesh points is adopted. The convergence criteria for this test case fulfills the condition that the maximum errors of all primitive variables between two adjacent iteration steps do not exceed 10^{-6}.

In the simulation, the Reynolds number varies from $\mathrm{Re} = 0.2$ to 5000. The corresponding Knudsen numbers computed from Eq. (59) are listed in Table III. As shown in this table, the cases of $\mathrm{Re} = 0.2, 0.5, 1$, and 2 lie in the transition flow regime; the cases of $\mathrm{Re} = 5, 10, 20$, and 50 belong to the slip flow regime; and the remaining ones of $\mathrm{Re} = 400, 1000, 2000$, and 5000 pertain to the continuum flow regime. For quantitative comparisons, two nondimensional parameters, i.e. the skin friction coefficient C_f and the drag coefficient C_d, are defined as

$$C_f = \frac{\tau_W}{\rho_\infty u_\infty^2/2} = \frac{\tau_W}{\gamma \mathrm{Ma}^2/4}, \tag{60}$$

$$C_d = \frac{1}{L_{\mathrm{BC}}}\int_0^{L_{\mathrm{BC}}} \left(C_f^{\mathrm{upper}} + C_f^{\mathrm{lower}}\right) dl, \tag{61}$$

where ρ_∞ and u_∞ are the free stream density and velocity, respectively. τ_W is the shear stress along the flat plate calculated by Eq. (6). C_f^{upper} and C_f^{lower} are the skin friction coefficients in the upper and the lower sides of the plate, respectively. In this test example, $C_f^{\mathrm{upper}} = C_f^{\mathrm{lower}}$ due to the symmetric distribution of the flow field to the flat plate.

Figure 12 shows the comparison of temperature contours around the flat plate in the transition and slip flow regimes obtained by the original and the present schemes. It can be seen that the results of the two schemes match very well with each other in the transition flow regime. However, in the slip flow regime, the temperature contours obtained by the conventional semi-implicit DVM start to deviate from the results of the present scheme, and the discrepancy becomes more evident as the Reynolds number is increased. To verify these results, a comparison between the present scheme and the UGKS [49] for flat plate flow at $\mathrm{Re} = 50$ is presented in Fig. 13. As shown in this figure, the temperature contours obtained by the present scheme basically agree with those of the UGKS, which demonstrates that the present results are more reasonable than the conventional semi-implicit DVM for this test example.

Quantitative comparisons are carried out in Fig. 14, which depicts the distribution of the skin friction coefficient on the flat plate and, in Fig. 15, which displays the drag coefficient of the flat plate with respect to the Reynolds number. In Fig. 15,

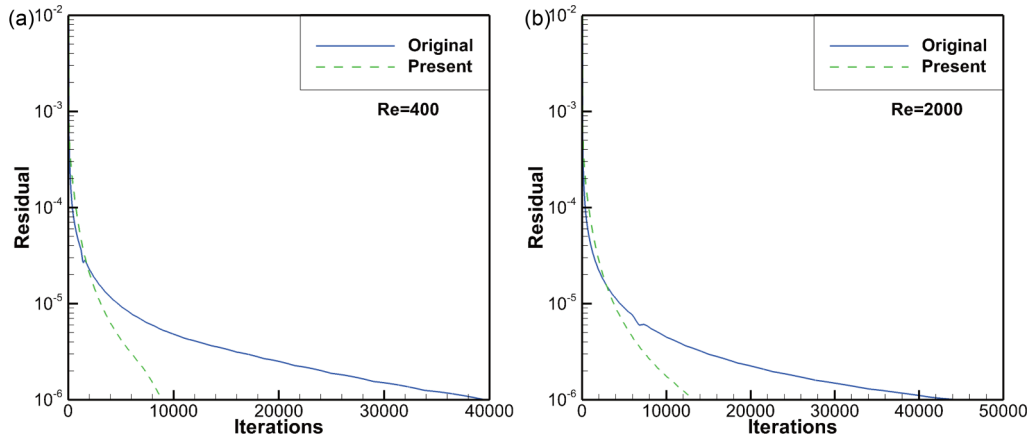

FIG. 19. Convergence history for flat plate flow in the continuum flow regime. (a) $\mathrm{Re} = 400$; (b) $\mathrm{Re} = 2000$.

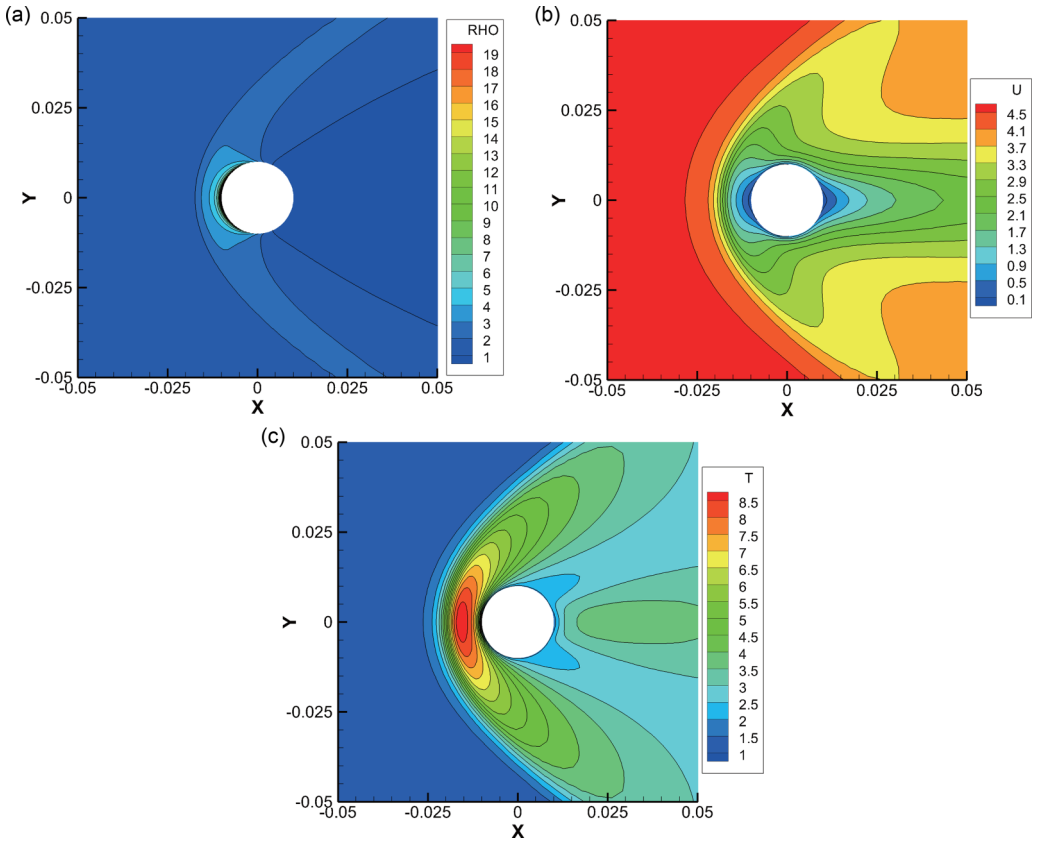

FIG. 20. Simulation results for hypersonic rarefied flow around a cylinder at Ma = 5 and Kn = 0.1. (a) Density contours. (b) u-velocity contours. (c) Temperature contours.

the fitting formula is given by [48,49]

$$\ln(C_d \cdot \mathrm{Ma}) = 0.225 - 0.333 \times \ln^2(\sqrt{\mathrm{Re}}/\mathrm{Ma}^{0.8}) + 0.031 \times \ln^3(\sqrt{\mathrm{Re}}/\mathrm{Ma}^{0.8}). \quad (62)$$

It can be observed that both the original and the present schemes give accurate prediction of the skin friction coefficient and the drag coefficient in the transition and the slip flow regimes [48,49].

Comparative study on the numerical efficiency is presented in Fig. 16 and Table III. In general, the present scheme shows higher convergence rate and consumes less computational time than the conventional semi-implicit DVM; and a higher speedup ratio can be expected when increasing the Reynolds number. The reason may be that the prediction step and the collision effect cast essential influence on the solutions of the test case with relatively high Reynolds number in which the particle collisions take place more intensively. It can then be inferred that in the transition and the slip flow regimes, the present scheme gives comparably accurate results as the original scheme, but is more competitive than the latter in terms of revealing physical details and computational efficiency.

Further investigations are performed in the continuum flow regime in which four cases of Re = 400, 1000, 2000, and 5000 are considered. Physical recognition hints that the particle collision effect plays an essential role in shaping the simulation results in this flow regime; therefore, the present improved implicit DVM should be more accurate than the conventional semi-implicit DVM. The numerical results well support such expectation. In Figs. 17 and 18, the skin friction coefficient and the drag coefficient computed by the conventional semi-implicit DVM significantly deviate from the reference data given by the Navier-Stokes solver [38] as the Reynolds number grows, while an appealing agreement is achieved by the present scheme in all cases. Moreover, in Fig. 19, we can see that the present scheme converges faster than the original one. As reported in Table III, a speed-up rate of 2.7 to 4.4 can be achieved in this flow regime. This evidence indicates that the present scheme is more accurate and efficient than the original one in the continuum flow regime.

D. Case 4: Hypersonic rarefied flow around a cylinder

In this section, the flow around a cylinder with the radius of $R_0 = 0.01$ m at Mach number of Ma = 5 and Knudsen number of Kn = 0.1 is solved to validate the present scheme for simulation of hypersonic rarefied flows. Consistent with previous study [30], in the present work, the reference density and temperature are, respectively, given by $\rho_0 = 8.582 \times 10^{-5}\,\mathrm{kg/m^3}$ and $T_0 = 273\,\mathrm{K}$, the temperature of the cylinder is fixed at T_0, and the reference viscosity is determined by

$$\frac{\mu_{\mathrm{ref}}}{R_0} = \frac{15\rho_0(2\pi RT_0)^{1/2}}{2(5-2w)(7-2w)}\mathrm{Kn}. \quad (63)$$

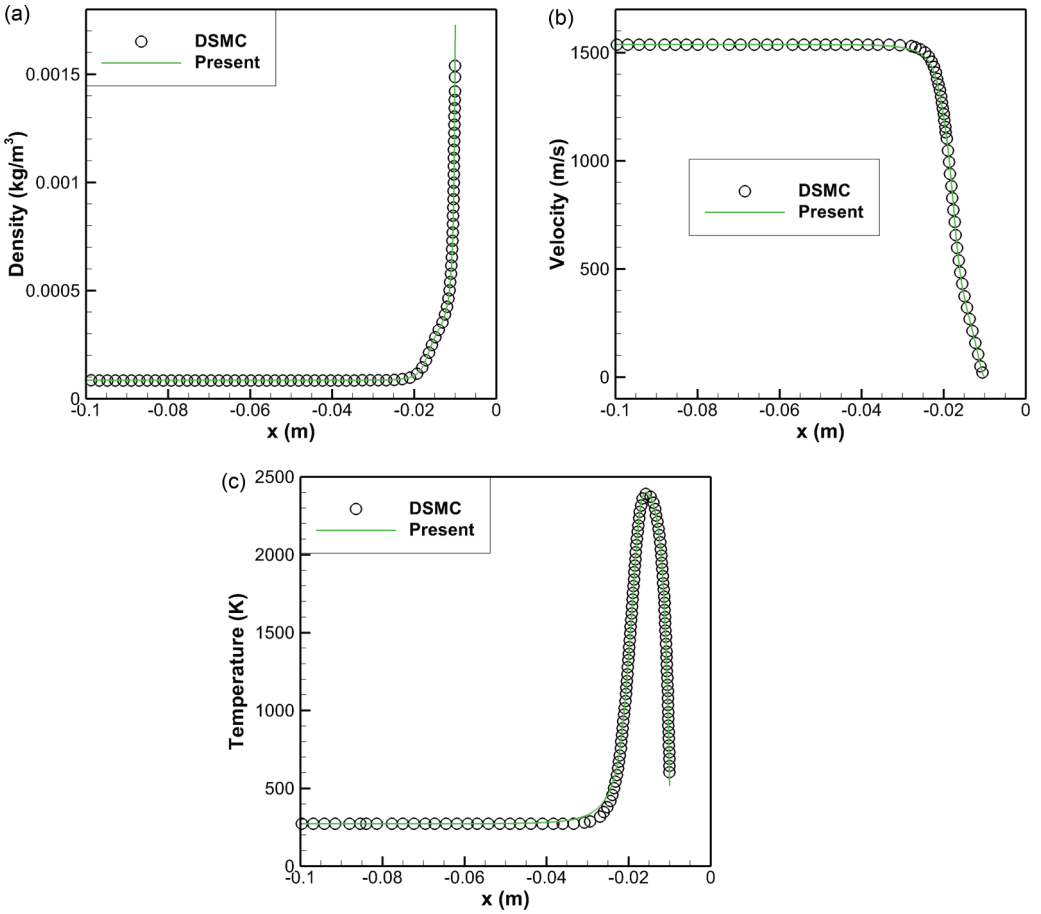

FIG. 21. Profiles along the stagnation line for hypersonic rarefied flow around a cylinder at Ma = 5 and Kn = 0.1. (a) Density. (b) u-velocity. (c) Temperature.

The collision timescale and the dynamic viscosity are, respectively, computed by Eq. (53) and Eq. (54), while the reference temperature T_{ref} is replaced by T_0 and the VHS model with $w = 0.81$ is utilized.

In the simulation, the CFL number for implicit discretization is set as $\sigma = 1$ for better numerical stability. For discretization of the particle velocity space, the Newton-Cotes quadrature with 101×101 mesh points uniformly distributed in $[-12, 12] \times [-12, 12]$ is utilized. In addition, a C-type mesh with 100 cells in the circumferential direction and 80 cells in the surface normal direction is used to discretize the physical space. The simulation results, including the contours, the profiles along the stagnation line in front of the cylinder, and the surface quantities, are shown in Figs. 20–22. Also displayed in Figs. 21 and 22 are the results of Zhu *et al.* [30] obtained by the direct simulation Monte Carlo (DSMC) method. Overall, the results of the improved implicit DVM agree well with the reference data [30], which demonstrates the capability of the present scheme for the simulation of hypersonic rarefied flows.

VI. CONCLUSIONS

An improved fully implicit discrete-velocity method (DVM) with an implicit prediction step is proposed in this paper. This method overcomes drawbacks of the conventional semi-implicit DVM and could give accurate and efficient solutions over the whole flow regimes. In this method, the equilibrium state is estimated by the prediction step, and both the distribution function and conservative variables at the cell center are simultaneously evolved in time. Such strategy facilitates the fully implicit discretization of the collision term in DVBE which can speed up the convergence rate. Another merit brought by the prediction step is the consideration of the particle collision effect. Solution accuracy in the continuum flow regime is thus enhanced in the present method while maintaining the inherent simplicity of the conventional semi-implicit DVM.

Four numerical examples, including the Sod shock tube problem, the lid-driven cavity flow, the flat plate flow, and hypersonic rarefied flow around a cylinder, are simulated for comprehensive evaluation of the proposed method in all flow regimes. Numerical results show that in the free molecular and the transition flow regimes, the prediction step has very little effect on the solutions. Thus, similar results are obtained by the original and the present schemes. But in the slip flow regime, the prediction step starts to take effect on the convergence rate of the calculation. Accordingly, the present scheme is more efficient than the original one. In the continuum flow regime, the prediction step dominates the solutions and the collision effect plays an important role in the calculation of numerical flux of the macroscopic governing equation. By

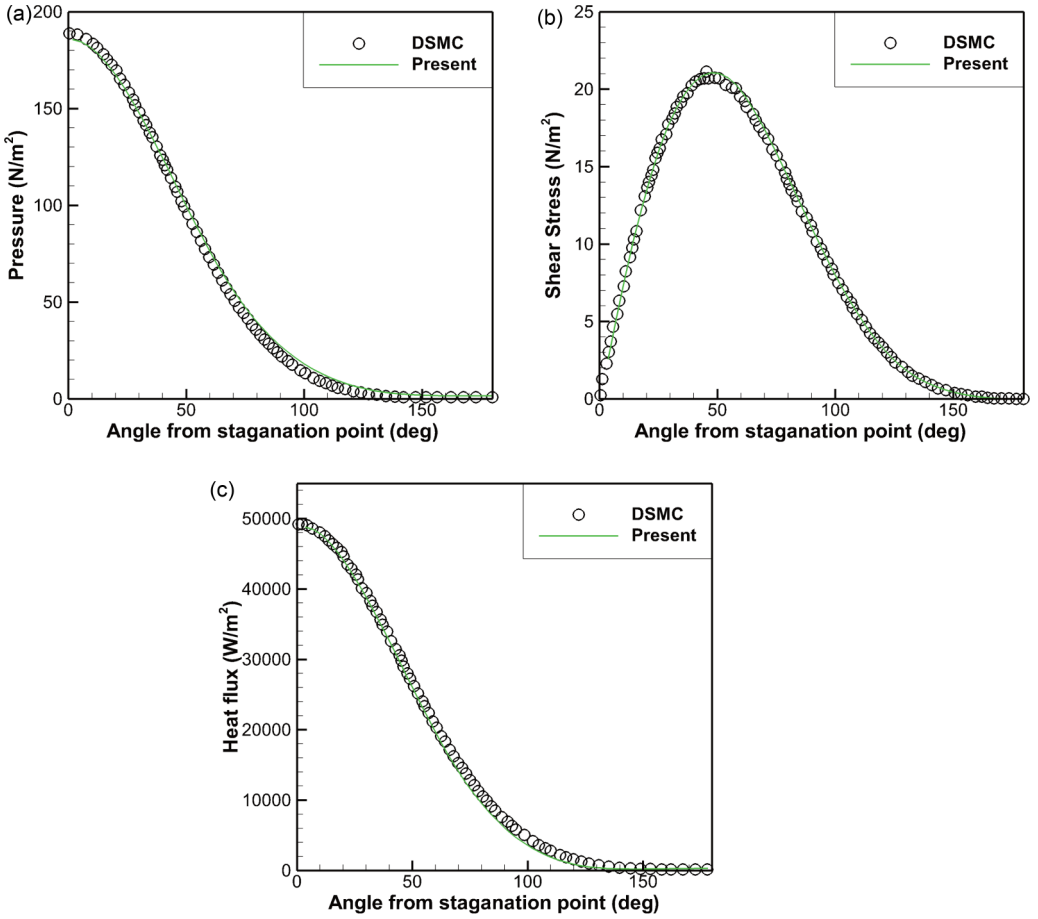

FIG. 22. Distribution of the surface quantities along the cylinder wall from the stagnation point to the trailing edge. (a) Pressure. (b) Shear stress. (c) Heat flux.

using the local solution of the Boltzmann equation with the collision term to reconstruct the macroscopic numerical flux, the present scheme automatically approaches to the Navier-Stokes solver in such regime. On the contrary, due to lack of the collision effect in the calculation of numerical flux, the conventional semi-implicit DVM cannot provide appealing solutions in the continuum flow regime.

ACKNOWLEDGMENTS

This work has been supported by the National Research Foundation Singapore, Sembcorp Industries Ltd., National University of Singapore under the Sembcorp-NUS Corporate Laboratory, and National Natural Science Foundation of China (Grants No. 11772157 and No. 11622219).

[1] G. A. Bird, *Molecular Gas Dynamics and the Direct Simulation of Gas Flows* (Clarendon, Oxford, 1994).
[2] D. Jiang, Study of the gas-kinetic scheme based on the analytic solution of model equations, Ph.D. thesis, China Aerodynamics Research and Development Center, 2016.
[3] K. Xu and C. Liu, A paradigm for modeling and computation of gas dynamics, Phys. Fluids **29**, 026101 (2017).
[4] Z. H. Li and H. X. Zhang, Gas-kinetic numerical studies of three-dimensional complex flows on spacecraft re-entry, J. Comput. Phys. **228**, 1116 (2009).
[5] L. Mieussens, Discrete-velocity models and numerical schemes for the Boltzmann-BGK equation in plane and axisymmetric geometries, J. Comput. Phys. **162**, 429 (2000).
[6] S. Z. Chen, K. Xu, and C. B. Lee, The dynamic mechanism of a moving Crookes radiometer, Phys. Fluids **24**, 111701 (2012).
[7] L. M. Yang, C. Shu, J. Wu, and Y. Wang, Comparative study of discrete velocity method and high-order lattice Boltzmann method for simulation of rarefied flows, Comput. Fluids **146**, 125 (2017).
[8] V. A. Titarev, Application of model kinetic equations to hypersonic rarefied gas flows, Comput. Fluids **169**, 62 (2018).
[9] C. K. Chu, Kinetic-theoretic description of shock wave formation. II, Phys. Fluids **8**, 1450 (1965).
[10] J. Y. Yang and J. C. Huang, Rarefied flow computations using nonlinear model Boltzmann equations, J. Comput. Phys. **120**, 323 (1995).
[11] K. Aoki, P. Degond, and L. Mieussens, Numerical simulations of rarefied gases in curved channels: Thermal creep, circulating flow, and pumping effect, Commun. Comput. Phys. **6**, 919 (2009).

[12] V. A. Titarev, Efficient deterministic modelling of three-dimensional rarefied gas flows, Commun. Comput. Phys. **12**, 162 (2012).

[13] L. M. Yang, C. Shu, J. Wu, and Y. Wang, Numerical simulation of flows from free molecular regime to continuum regime by a DVM with streaming and collision processes, J. Comput. Phys. **306**, 291 (2016).

[14] V. V. Aristov, *Direct Methods for Solving the Boltzmann Equation and Study of Nonequilibrium Flows* (Springer Science & Business Media, New York, 2012).

[15] Z. H. Li and H. X. Zhang, Study on gas kinetic unified algorithm for flows from rarefied transition to continuum, J. Comput. Phys. **193**, 708 (2004).

[16] S. Pieraccini and G. Puppo, Implicit-explicit schemes for BGK kinetic equations, J. Sci. Comput. **32**, 1 (2007).

[17] V. A. Titarev, Conservative numerical methods for model kinetic equations, Comput. Fluids **36**, 1446 (2007).

[18] A. N. Kudryavtsev and A. A. Shershnev, A numerical method for simulation of microflows by solving directly kinetic equations with WENO schemes, J. Sci. Comput. **57**, 42 (2013).

[19] K. Aoki, K. Kanba, and S. Takata, Numerical analysis of a supersonic rarefied gas flow past a flat plate, Phys. Fluids **9**, 1144 (1997).

[20] V. A. Titarev, Numerical method for computing two-dimensional unsteady rarefied gas flows in arbitrarily shaped domains, Comput. Math. Math. Phys. **49**, 1197 (2009).

[21] V. A. Titarev, Implicit numerical method for computing three-dimensional rarefied gas flows on unstructured meshes, Comput. Math. Math. Phys. **50**, 1719 (2010).

[22] L. Mieussens, Discrete velocity model and implicit scheme for the BGK equation of rarefied gas dynamics, Math. Models Methods Appl. Sci. **10**, 1121 (2000).

[23] K. Xu and J. C. Huang, A unified gas-kinetic scheme for continuum and rarefied flows, J. Comput. Phys. **229**, 7747 (2010).

[24] J. C. Huang, K. Xu, and P. B. Yu, A unified gas-kinetic scheme for continuum and rarefied flows II: Multi-dimensional cases, Commun. Comput. Phys. **3**, 662 (2012).

[25] K. Xu, *Direct Modeling for Computational Fluid Dynamics: Construction and Application of Unified Gas-Kinetic Schemes* (World Scientific, Singapore, 2015).

[26] Z. Wang, H. Yan, Q. B. Li, and K. Xu, Unified gas-kinetic scheme for diatomic molecular flow with translational, rotational, and vibrational modes, J. Comput. Phys. **350**, 237 (2017).

[27] Z. L. Guo, K. Xu, and R. J. Wang, Discrete unified gas kinetic scheme for all Knudsen number flows: Low-speed isothermal case, Phys. Rev. E **88**, 033305 (2013).

[28] Z. L. Guo, R. J. Wang, and K. Xu, Discrete unified gas kinetic scheme for all Knudsen number flows: II. Thermal Compressible case, Phys. Rev. E **91**, 033313 (2015).

[29] C. Wu, B. C. Shi, Z. H. Chai, and P. Wang, Discrete unified gas kinetic scheme with a force term for incompressible fluid flows, Comput. Math. Appl. **71**, 2608 (2016).

[30] L. H. Zhu, Z. L. Guo, and K. Xu, Discrete unified gas kinetic scheme on unstructured meshes, Comput. Fluids **127**, 211 (2016).

[31] Y. Zhu, C. Zhong, and K. Xu, Implicit unified gas-kinetic scheme for steady state solutions in all flow regimes, J. Comput. Phys. **315**, 16 (2016).

[32] P. Wang, M. T. Ho, L. Wu, Z. Guo, and Y. Zhang, A comparative study of discrete velocity methods for low-speed rarefied gas flows, Comput. Fluids **161**, 33 (2018).

[33] L. M. Yang, C. Shu, W. M. Yang, and J. Wu, An implicit scheme with memory reduction technique for steady state solutions of DVBE in all flow regimes, Phys. Fluids **30**, 040901 (2018).

[34] S. Chen, Z. Guo, and K. Xu, Simplification of the unified gas kinetic scheme, Phys. Rev. E **94**, 023313 (2016).

[35] P. L. Roe, Approximate Riemann solvers, parameter vectors, and difference schemes, J. Comput. Phys. **43**, 357 (1981).

[36] E. F. Toro, M. Spruce, and W. Speares, Restoration of the contact surface in the HLL Riemann solver, Shock Wave **4**, 25 (1994).

[37] L. M. Yang, C. Shu, and Y. Wang, Development of a discrete gas-kinetic scheme for simulation of two-dimensional viscous incompressible and compressible flows, Phys. Rev. E **93**, 033311 (2016).

[38] L. M. Yang, C. Shu, and J. Wu, A hybrid lattice Boltzmann flux solver for simulation of viscous compressible flows, Adv. Appl. Math. Mech. **8**, 887 (2016).

[39] E. M. Shakhov, Generalization of the Krook kinetic relaxation equation, Fluid Dyn. **3**, 95 (1968).

[40] S. Yoon and A. Jameson, Lower-upper symmetric-Gauss-Seidel method for the Euler and Navier-Stokes equations, AIAA J. **26**, 1025 (1988).

[41] J. Blazek, *Computation Fluid Dynamics: Principles and Applications*, 3rd ed. (Butterworth-Heinemann, Oxford, UK, 2015).

[42] B. Van Leer, Towards the ultimate conservative difference scheme. IV. A new approach to numerical convection, J. Comput. Phys. **23**, 276 (1977).

[43] K. Xu, To overcome memory barrier of kinetic solvers for non-equilibrium flow study, Sci. Bull. **62**, 99 (2017).

[44] U. Ghia, K. N. Ghia, and C. T. Shin, High-Re solutions for incompressible flow using the Navier-Stokes equations and a multigrid method, J. Comput. Phys. **48**, 387 (1982).

[45] C. B. Lee, New features of CS solitons and the formation of vortices, Phys. Lett. A **247**, 397 (1998).

[46] C. B. Lee, Possible universal transitional scenario in a flat plate boundary layer: Measurement and visualization, Phys. Rev. E **62**, 3659 (2000).

[47] C. B. Lee and S. Fu, On the formation of the chain of ring-like vortices in a transitional boundary layer, Exp. Fluids **30**, 354 (2001).

[48] Q. Sun and I. D. Boyd, Drag on a flat plate in low-Reynolds-number gas flows, AIAA J. **42**, 1066 (2004).

[49] Y. Zhu, C. Zhong, and K. Xu, Unified gas-kinetic scheme with multigrid convergence for rarefied flow study, Phys. Fluids **29**, 096102 (2017).